Journal of Hydrology 638 (2024) 131267

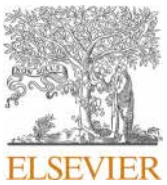

Contents lists available at ScienceDirect

Journal of Hydrology

journal homepage: www.elsevier.com/locate/jhydrol

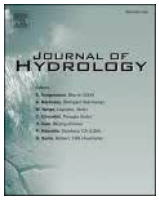

Research papers

Transit time tracing using wetness-adaptive StorAge Selection functions—application to a Mediterranean catchment

Nico Hachgenei *, Guillaume Nord, Lorenzo Spadini, Patrick Ginot, Céline Voiron, Céline Duwig

University Grenoble Alpes, CNRS, INRAE, IRD, Grenoble INP, IGE, Grenoble, France

ARTICLE INFO

This manuscript was handled by Marco Borga, Editor-in-Chief, with the assistance of Yuting Yang, Associate Editor

Keywords:
StorAge Selection function
Transit time distribution
New water fraction
Mediterranean climate
Flash flood
Contaminant

ABSTRACT

Not just the quantities but also the transit times are of crucial importance for understanding the transfer of water through a catchment. This information is essential, for example, for determining the risk of the transfer of contaminants from diffuse, agricultural sources toward surface water bodies. We created a hydrological age-tracking reservoir model of a *meso*-scale Mediterranean catchment that is prone to flash floods. We implemented StorAge Selection (SAS) functions that adapt to the catchment's wetness condition in order to represent changing flow processes. The goal is to evaluate the evolution of transit time distributions (TTDs) through the catchment (1 h time step, 1 h resolution), providing an example for a rural catchment under a Mediterranean climate. The focus is on flood events, and the results are interpreted with regard to the risk of contaminant transfer from diffuse sources. The dependence of water age preferences on catchment wetness is examined. We propose and test a multi-tracer approach to parametrize SAS functions on multiple reservoirs.

The model was calibrated and validated against the streamflow discharge (Q), deuterium isotope signature (δ^2H) and dissolved silica concentration ($[Si]$) at the outlet. While δ^2H acted as a direct tracer of rain-water, $[Si]$ was used as a tracer of the contact time with the soil and rock minerals. The model revealed high event water fractions during flood events (with up to 63 % of water younger than one day) and a dominance of water older than one year most of the remaining time. This suggests an elevated risk of the transfer of agricultural contaminants toward streams during flood events. The results also indicate an inverse storage effect (ISE), with young water preferences increasing under wet conditions.

1. Introduction

In classical hydrological modeling, e.g., for flood and drought forecasting, the variable of interest is the discharge of water leaving the catchment via streamflow at the outlet. These classical models are calibrated based on water quantities only (e.g., the streamflow discharge, ground-water level and/or soil moisture). In the real world, the streamflow discharge is often controlled by celerity (pressure wave propagation) instead of mass transfer (Hrachowitz et al., 2016). This means that an increased streamflow caused by a rain event does not necessarily consist of water from this rain event but may consist of older water pushed into the stream by the arriving new water. A classical hydrological model may very well reproduce time series of the streamflow discharge from observed precipitation without providing any information on the history of the water that this streamflow consists of.

In order to understand the transfer of water and matter through a catchment, it is not sufficient to reproduce the correct streamflow discharge at the catchment's outlet. The temporal component of the transfer of water (the transit time) can be of crucial importance. This is particularly true with regard to the risk of contaminant transfer from soils toward streams. During slow transfer, many of these compounds may be adsorbed to soil surfaces and/or degraded, while transfer via rapid flow processes (preferential flow, overland flow and flow through macropores) may represent an elevated risk of transfer of these compounds into surface water bodies (Jarvis, 2007; Singh and Stenger, 2018).

The transit time of water cannot be measured directly. However, at smaller scales (up to the hillslope scale), experimental methods to estimate transit time distributions (TTDs) and age preferences exist, e.g., the PERTH method (Kim et al., 2022; Harman and Kim, 2014). These

* Corresponding author.
E-mail address: nico.hachgenei@univ-grenoble-alpes.fr (N. Hachgenei).

https://doi.org/10.1016/j.jhydrol.2024.131267
Received 17 May 2023; Received in revised form 1 March 2024; Accepted 22 March 2024
Available online 23 May 2024

methods rely on the controlled input of water and tracers and are therefore difficult/impossible to apply at the catchment scale. At this scale, hydrological modeling is the tool that allows one to obtain insights on water transit times.

1.1. Age tracking in hydrological models

Transit time modeling has become an important discipline in hydrological modeling in the recent past due to the increasing computational power and accessibility of analytical methods, particularly low-cost optical methods for stable isotope ratios. Observations of environmental tracers allow one to extract the mass transfer of water from precipitation-discharge relationships and disentangle it from celerity (Sprenger et al., 2019). Different tracers have been used to track the age of water.

The transit times of water can be defined in the form of TTDs, which represent the portion of water experiencing each transit time. The TTD can be expressed in a forward or backward way; these distributions would be equal in a steady-state system but differ significantly in a catchment with unsteady fluxes (Rinaldo et al., 2015). The forward notation represents the distribution of time that the water from one rain event would stay in the catchment until leaving it. The backward notation represents the distribution of time that a volume of water leaving the catchment at one particular moment took to transit it. Both the forward and backward notations can be of interest (Botter et al., 2011; Benettin et al., 2015b). The forward notation is of interest when investigating the fate of water and/or contaminants injected into the system at a certain time, while the backward TTD characterizes the water in the stream and corresponds to "analyzing" the history of a water sample taken in the stream at a certain moment.

Regarding contaminants, science is often particularly concerned with their presence in surface water bodies (Singh and Stenger, 2018; Obimakinde et al., 2017; Charuaud et al., 2019; Ojoghoro et al., 2021). A high risk of the transfer of contaminants of agricultural origin (e.g., pesticides, veterinary pharmaceuticals, nutrients) from the soil surface into surface water bodies is expected during periods with a high percentage of very young water in the stream (Jarvis, 2007; Singh and Stenger, 2018). In the following, the backward notation of the TTD is used, since it enables one to identify the periods with a predominance of very young water in the stream. The backward TTD of the streamflow leaving a catchment corresponds to the water's age distribution in this flow Q, where $Q(T,t)$ is the absolute age distribution in units of water height or volume per time and $p_Q(T,t) = \frac{Q(T,t)}{Q(t)}$ is its unitless probability density function (pdf). Both represent distributions over age T at a time t. T equals zero at the time when a volume of water enters the system in the form of effective precipitation (excluding interception) and then increases with time. The cumulative distribution function (cdf) is denoted by $P_Q(T,t) = \int_{T=0}^{\infty} p_Q(T,t)$.

This water age distribution exists for any flux of water leaving a reservoir or catchment. Inside a reservoir S, the water age distribution is denoted by $S(T,t)$, $p_S(T,t)$ or $P_S(T,t)$ (absolute, pdf or cdf respectively). The catchment's overall water age distribution corresponds to the residence time distribution (RTD) of water in the catchment.

Early approaches to tracking transit times through hydrological catchments include the steady-state TTD, which assumes a time-invariant mathematical shape (e.g., exponential or gamma distribution) for the TTD (McGuire and McDonnell, 2006; Małoszewski and Zuber, 1982; Kirchner et al., 2000, 2001).

The parameters of this distribution were calibrated against observed tracer time series in the system outflow. Different modifications have been made to these TTDs in order to account for non-steady-state conditions, e.g., by presenting the TTD as a function of the cumulative flow volume instead of time (Niemi, 1977; Rodhe et al., 1996), assuming time-invariant flow-paths but allowing time-variant flow.

An elegant way to avoid having to adapt rigid TTDs to time-variant conditions is to define the age selectivity of a catchment or reservoir instead of the TTD. This approach is today well-known as the use of StorAge Selection (SAS) functions (Hrachowitz et al., 2016; Rinaldo et al., 2015; Sprenger et al., 2019). SAS functions define the relation between the water age distributions in a reservoir and in a flux leaving the reservoir in a spatially integrated manner. They can be described as the equivalent of the advection–dispersion equation along the dimension of age, integrated over space (Fiori and Russo, 2008; Ginn et al., 2009; Rinaldo et al., 2015). They were initially defined by Botter et al. (2011), who called them mixing functions (Eq. (1)):

$$\omega_Q(T,t) = \frac{p_Q(T,t)}{p_S(T,t)} \tag{1}$$

The SAS functions define the preference of a flux for water of different ages from a reservoir instead of the proportions of water of each age in the flux. Thereby, they adapt to variable age distributions in the reservoir (if very little young water is present, very little can be taken, even if the flux has a high preference for young water). Water fluxes coming out of different reservoirs have different probabilities to take older versus younger water. This can be due to the location of the water in the reservoir (e.g., on a vertical axis, along a hillslope, in smaller versus larger pores of the soil, closer or further from plant roots, etc.).

While for any flux, a real SAS function exists, in hydrological modeling, mathematical functions that can be parameterized to reproduce tracer observations are used to approximate them. SAS functions are well adapted for implementation in conceptual models, as they represent the spatial heterogeneity of the hydrologic features of the critical zone by integrating their functionality without the need to explicitly specify them (Botter et al., 2011).

A more physically and spatially explicit way of tracking water age is to track water particles throughout spatially distributed hydrologic models (Davies et al., 2013; Maxwell et al., 2016; Danesh-Yazdi et al., 2018; Remondi et al., 2018; Yang et al., 2018; Weill et al., 2019). These models are more demanding in terms of computational power and need detailed spatial data concerning the structure and composition of the critical zone, but in return they can provide spatially distributed insights into water transfer dynamics.

Kim et al. (2022) experimentally determined the SAS function on artificial hillslopes using repeated simulated precipitation events with different tracers. They found a general old water preference, which is increased under wet conditions. Similar results were presented by Meira Neto et al. (2022) based on bench-scale experiments. This is contrary to catchment-scale modeling studies that mostly find young water preferences (Benettin et al., 2017; Berghuijs and Allen, 2019). In addition, catchment-scale studies tend to find an increased preference for young water under wetter conditions (Benettin et al., 2017; Harman, 2015; Rodriguez et al., 2018). The difference in the young versus old water preferences of those systems may be explained by heterogeneity and scale among other factors: The high homogeneity of the artificial, smaller-scale systems lead to more homogeneous, advective transport, while a heterogeneous, natural system has more preferential flow paths, leading to younger water bypassing the slow compartments (soil matrix) and directly leaving the system. Furthermore, at a larger scale, different factors and flow processes become relevant (flow concentration in the drainage network, flat vs. steep slopes, diversity of surfaces) that again lead to more heterogeneity between the slow soil and ground-water reservoirs on the one hand and the rapid stream, preferential subsurface and overland flow (OF) on the other hand (Berghuijs and Allen, 2019; Blöschl, 2001). Regarding the effect of wetness on the age preference, in a homogeneous artificial system with relatively constant flow paths under controlled conditions, the highest wetness occurs during irrigation when a large quantity of young water is stored and infiltrated vertically, while mainly older water is pushed out, corresponding to a preference for old water. Under drier conditions (meaning after a period without irrigation), water from the last event has advanced downslope

and is contributing to the outflow, corresponding to a less pronounced old water preference (Kim et al., 2022). In a natural, heterogeneous catchment, preferential flow paths (OF, macropore flow) are activated during precipitation events or under wet conditions, leading to a younger water preference under these conditions (Harman, 2015). These differences show that observations on a reduced scale cannot be applied directly to the catchment scale. Therefore, in order to understand water transfer at the catchment scale, tracer-based hydrological models remain the preferable tool.

The increased young water preference under wet conditions is known as the inverse storage effect (ISE) (Harman, 2015; Rodriguez et al., 2018). The ISE can be explained by the activation of more preferential flow paths under wetter conditions, leading to a stronger young water preference through the bypassing of the slower components of the reservoir (Harman, 2015). The ISE has been confirmed by studies under temperate oceanic climates (Benettin et al., 2015a; Harman, 2015; Benettin et al., 2017). Transit times (mean and TTD) are studied more often than age preferences. A decrease in the transit time under wetter conditions has been observed in many studies (Botter et al., 2010; Gallart et al., 2020; Heidbüchel et al., 2012; Hrachowitz et al., 2013; Hrachowitz et al., 2015a; Klaus et al., 2015; Rinaldo et al., 2011; Segura et al., 2012; Soulsby et al., 2015; van der Velde et al., 2015). This decrease in the transit time is, however, not sufficient to confirm the ISE, as under wet conditions the water in storage is also younger.

In order to represent storage-dependent age preferences at the catchment scale, different approaches exist. Conceptual models with multiple reservoirs with varying contributions to the streamflow can produce varying age preferences at the catchment scale. This is the case even for reservoirs with a fixed age preference (Rodriguez et al., 2021) or with no age preference (complete mixing hypothesis; Rodriguez et al., 2018). SAS functions can also be made time-variant as a function of the current wetness conditions. Harman (2015) use wetness-adaptive SAS functions by making the SAS function's scale parameter dependent on the difference in storage compared to its mean, multiplied by a calibrated linear factor.

Transit time tracing studies often focus on longer periods that range from months to years. Remondi et al. (2019) compare modeled transit times in synthetic catchments under different climates and with different topographies. They show that under a wet climate, the transit time is generally linked to discharge through topographic characteristics. Under a dry climate, the transit time is much more variable and cannot be directly linked to the topography. They conclude that under dry conditions (semi-arid and Mediterranean climate), the variable climate determines the TTD more strongly than the topography.

The Mediterranean climate is characterized by extended dry periods and intense precipitation events, generating a very dynamic hydrology with intermittent streams, OF and flash floods (Nuissier et al., 2008; Delrieu et al., 2005). Gallart et al. (2020) investigated transit time distributions in a Mediterranean catchment in the south eastern Pre-Pyrenees (Spain) using the ratio of the amplitude of isotope signatures in the stream and precipitation. They found increasing young water fractions with an increased discharge of up to 100 % of the water being less than 2–3 months old during the strongest flood events. Rodriguez et al. (2018) studied the relationship between catchment storage and the TTD in a forested headwater catchment in Oregon (USA) under a Mediterranean climate. They used a conceptual model with multiple reservoirs, and within each reservoir, they applied the complete mixing hypothesis (no age preference). They calibrated the model using observed $\delta^{18}O$ values and calculated the overall SAS function under different conditions a posteriori. They obtained an old water preference under dry conditions and a young water preference under wet conditions, confirming the ISE. They conclude that under a Mediterranean climate it is important to consider wetness-dependent variable flow paths, which lead to variable transit times.

1.2. Knowledge gap and goal of this study

To the authors' knowledge, little transit time tracing has been done under a Mediterranean climate at a high temporal resolution, and none has been done in rural catchments with agricultural land use. The goal of this study is to investigate the TTD of the Claduègne catchment (see subsection 2.1) under a Mediterranean climate and its evolution over the seasons and in particular throughout flood events at a high temporal resolution. The catchment is prone to flash floods and has a time of concentration of four to five hours (Hachgenei, 2018). This study also aims to validate whether the ISE can be observed in this agricultural catchment under a Mediterranean climate, as was found by Rodriguez et al. (2018) for a forested catchment under a Mediterranean climate. The SAS functions are mostly assumed to be constant (e.g. Benettin et al., 2017; Zhang et al., 2021); however, flow processes are known to differ with variable wetness conditions (Harman, 2015). These variations in flow processes are expected to affect the flow's age preference. Therefore, we created an age tracking model of the Claduègne catchment based on SAS functions that adapt to the wetness conditions. We evaluate if these adaptive SAS functions improve the model fit without additional degrees of freedom (same number of parameters). The catchment's rapid dynamics require a small model time step (1 h) and a high tracer sampling frequency during flood events (up to 2 h^{-1}). The study is part of an investigation of the risk of the transfer of contaminants from diffuse agricultural sources toward streams under Mediterranean conditions. The resulting TTDs will therefore be interpreted with regard to their implications for the risk of contaminant transfer. As explained above, a rapid transfer of event water into streams induces an elevated risk of contaminant transfer to the streams. Therefore, the focus is on event water reaching the streams; in particular, the focus is on water aged less than one day (new water fraction [nwf]) and also water aged less than 30 days (young water fraction [ywf]). Risk periods are identified by investigating the evolution of the nwf and ywf over time. An emphasis is placed on the representation of flood events, which account for a large portion of the annual streamflow volume in this environment. Equifinality is a concern, especially in conceptual modeling, where different parameter sets can represent observed (discharge and tracer) data equally well. In order to evaluate the robustness of the modeled TTDs with regard to this equifinality, we compare the age results of a selection of contrasted parameter sets that produce a good fit.

2. Methods and data

2.1. Study site

The Claduègne catchment (42 km^2) is situated in the French Ardèche department (44.562202°N, 4.478961°E, Fig. 1). It is part of the *Cévennes-Vivarais Mediterranean Hydrometeorological Observatory (OHM-CV)* and presented in detail in Nord et al. (2017). It also belongs to the *Observatoires de la Zone Critique: Applications et Recherche (OZCAR)* research infrastructure (Gaillardet et al., 2018). It is situated on two contrasting geologies, with the northern upstream part on the Coiron basaltic plateau and the southern downstream part on sedimentary marly-limestone bedrock (50 % of the total catchment area each). These two parts contraste with regard to precipitation amounts and intensities, potential evapotranspiration and soil types and altitude. The catchment's altitude ranges from 205 to 831 m.a.s.l. The principal types of land cover are pastures for livestock, cultivated soils (vineyards and cereals), small forests, shrubland and villages. Population densities are low (from 8.5 hab km^{-2} on the Coiron plateau to 117.9 hab km^{-2} in Villeneuve de Berg, the largest village in the catchment; calculated from INSEE (2017)). The catchment's median slope is 14.3 %.

The catchment is exposed to a Mediterranean climate and prone to flash floods. The Mediterranean climate is characterized by a dry summer, followed by frequent intense precipitation events in autumn and

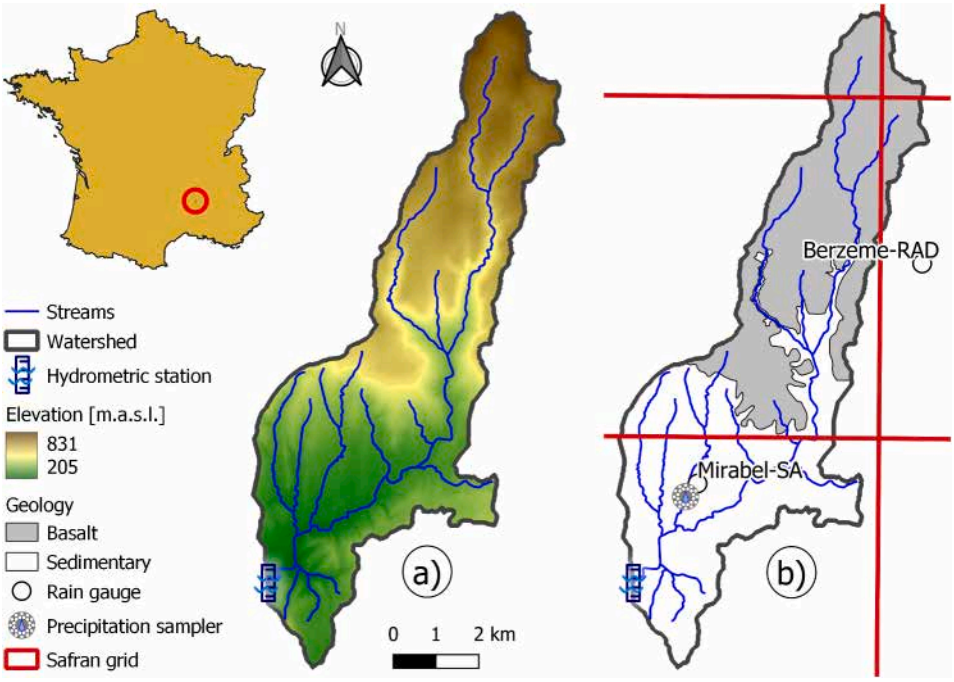

Fig. 1. Map of the Claduègne catchment: a) elevation, b) geology and measuring stations.

occasionally in spring (Nuissier et al., 2008; Boudevillain et al., 2011, 2016). Snow rarely occurs. Precipitation events of more than 200 mm in 24 h have a return period of 5–10 years in the Claduègne catchment (Beuerle, 2021). Fig. 2a shows the monthly distribution of discharge values at the outlet of the Claduègne catchment. The monthly average values vary by almost two orders of magnitude, and the observed discharge varies from 10 l s^{-1} during dry summers to more than 100 m^3/s during strong flood events. The year can be divided into two seasons: a humid season (above average discharge) from October to May and a dry season (below average discharge) from June to September. Fig. 2b shows the cumulative distribution of the streamflow discharge as time and volume fractions. It shows that strong flood events account for a large fraction of the streamflow volume while only taking a small fraction of time. One third of the streamflow volume leaves the catchment in 1.4 % of the time.

2.2. Data

The dataset used as the model input consists of an hourly timeseries of the following variables: 1) P_{BER} and P_{MIR} are the observed hourly precipitation (aggregated from 6-minute observation time step) at the Berzeme-RAD and Mirabel-SA meteorological stations (Météo France), respectively (Fig. 1b). They are used in the model as the precipitation on the Coiron plateau and the sedimentary part of the catchment, respectively. 2) E_{pBER} and E_{pMIR} are the potential evapotranspiration of the two parts of the catchment corresponding to each geological entity. For the period from August 2017 to July 2020, they are calculated from hourly reanalysis data (radiation, air temperature, humidity and wind speed) from the *Système d'Analyse des Renseignements Adaptés à la Nivologie (SAFRAN)* model (Vidal et al., 2010) using the formula from Allen et al. (1998). The *SAFRAN* grid cells (8·8 km^2) are shown in Fig. 1b, and the values for each geological entity are calculated by weighting the values

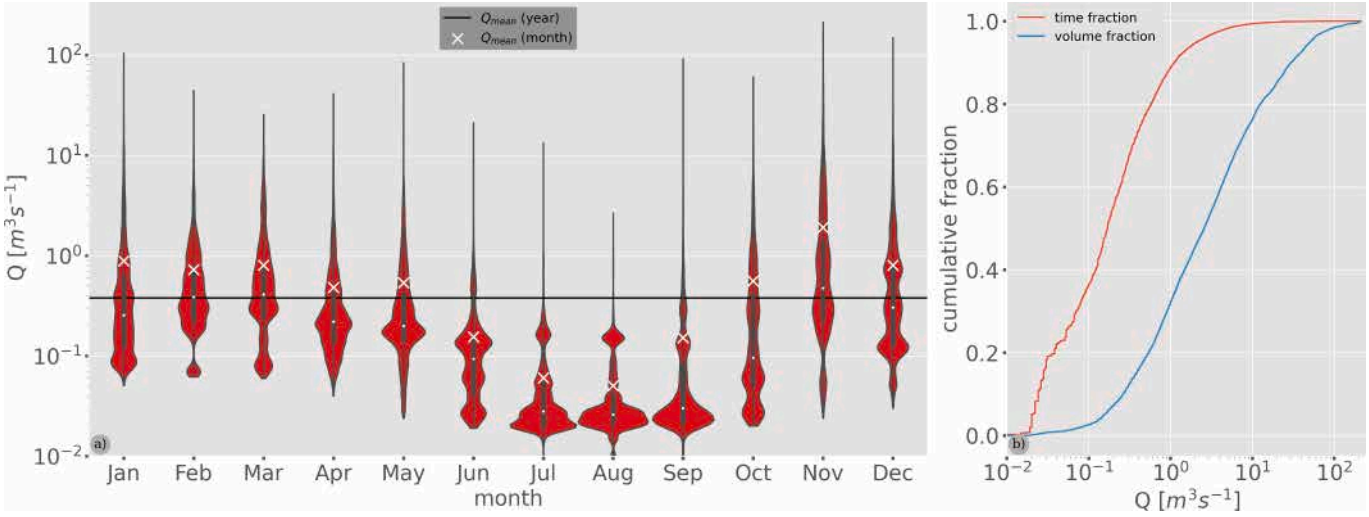

Fig. 2. A) monthly distribution of discharge values at the Claduègne outlet. b) cumulative distribution of streamflow discharge at the Claduègne outlet as time and volume fractions.

of each grid cell by the proportion of the entity's area covered by the respective grid cell. For the remaining period (beginning of 2017 and end of 2020), daily data interpolated to the two Météo France stations (Berzème and Mirabel) are used (calculations done by Météo France), because SAFRAN reanalysis data were not available. 3) δ^2H_P is the precipitation deuterium isotopic ratio in terms of the relative deviation from Vienna Standard Mean Ocean Water (VSMOW). This was obtained from continuous precipitation samples of 5 mm of precipitation each taken using a *Teledyne ISCO 3700* automated sampler connected to a rain gauge (Fig. 1b) and controlled by a *Campbell CR800* datalogger, averaged to hourly values. If no precipitation occurred for 3 h and the current sample contained at least 2 mm, a new sample was started. Precipitation sampling started in October 2019. For the period before October 2019 (used as spin-up), monthly averages from the observation period are used. δ^2H_P of periods without samples (e.g. due to a filled sampler) were set to the next valid sample's value.

The model calibration and validation data consist of time series of the following three parameters at the outlet of the Cladugne catchment: 1) Q_{obs}, which is the observed streamflow discharge (water level from radar and rating curve), measured at a 10-minute resolution and averaged to an hourly resolution (OHMCV, 2011); 2) δ^2H_S; and 3) $[Si_S]$, which represents the observed stream deuterium isotopic ratio [‰] and dissolved silica concentration (expressed in mg Si per L) from samples taken at variable frequency. Stream water sampling started in June 2019. Over several two-week periods covering all seasons, a sample was taken every 12 h using an *ISCO 1680* automated sampler. In addition, during flood periods (defined by seasonally adapted thresholds for the water level and turbidity), samples were taken every 30 min by a *Teledyne ISCO 3700* automated sampler. Only hours containing a sample are assigned a value; hours containing two samples are assigned the average value.

Before analysis, all samples were filtered at 0.45 μm using *Sartorius Minisart NML* cellulose acetate filters and stored at 4 °C. The δ^2H-analysis was performed by using a *Picarro L2140-i* isotopic water analyzer and applying an asymptotic correction of the memory effect, as described in Hachgenei et al. (2022). $[Si]$ was analyzed using inductively coupled plasma – optical emission spectrometry (ICP-OES; *Varian 720-ES*).

2.3. The model

We developed and used a continuous, semi-distributed hydrological model that tracks water throughout the Cladugne catchment from the moment it enters the system as rainfall until it leaves the catchment through the outlet at a time step of 1 h (Hachgenei et al., 2023). The time step of 1 h was chosen as a good compromise in order to limit the use of numerical resources (calculation time and size of age tracking results) on the one hand and maintain a good representation of the dynamics of rapid flood events on the other hand. The basic model structure is similar to that of the model used by Fovet et al. (2014); Hrachowitz et al. (2014); Hrachowitz et al. (2015). The unique identifier of each volume of water is its age, i.e., the time that has passed since the moment it entered the catchment in the form of effective precipitation onto the soil surface. The model is semi-distributed, as it integrates hydrological processes spatially over each of the two geological entities of the Cladugne catchment: the Coiron plateau on a basaltic geology (upstream) and the lower part on a sedimentary geology (marl and limestone). Within each geological entity, there are two non-linear reservoirs and a small interception reservoir. The two entities are subjected to different precipitation and potential evapotranspiration, but the same hydrological parameters are applied to the corresponding reservoirs in both geologies in order to limit the number of calibrated parameters. Only the silica dissolution rate constants (see subsection 2.3.3) are parametrized individually due to the difference in the geology. Water fluxes between and out of the reservoirs are calculated as a function of the amount of water in the reservoir. The reservoirs represent different parts of the critical zone, from the canopy to groundwater. Their functioning with regard to water transfer is conceptualized in a spatially integrated way, but they do not possess clearly defined spatial boundaries. Each reservoir has at least one flux entering it and one flux leaving it. In both the reservoirs and the fluxes, the age of each volume of water is tracked. Each flux can have a preference for younger or older water, which is implemented via SAS functions. The observed discharge Q at the catchment's outlet, as well as tracer concentrations (δ^2H and $[Si]$), are used to calibrate the model and evaluate its performance. Once the model performs well in reproducing Q and the tracer dynamics, the age distributions of the streamflow at any time during the simulated period can be obtained at a 1 h resolution. The model is split into two versions: (1) The first is a tracer model that only calculates current-state age information and therefore runs rapidly. The tracer model is run many times for calibration. (2) The second is an age tracking model that stores and outputs the water age information of all reservoirs and fluxes at any time. This version takes much longer to run and is only run once with the parameter set obtained from calibration. In the following, the general model structure and its functioning with regard to the age of water are explained; then, the particularities of the tracer model and the age tracking model are described in detail.

2.3.1. Model structure

Each of the two geological entities of the catchment contains the following three reservoirs (Fig. 3):

1. The interception reservoir S_i: S_i has a limited capacity I_{max} and receives all precipitation until it is full. All further precipitation (effective precipitation P_e) goes directly into the unsaturated reservoir S_u. Water from S_i never reaches the soil. The only flux leaving S_i is the evaporation E_i.
2. The unsaturated reservoir S_u: S_u represents the unsaturated zone and includes the soil matrix, as well as rapid flow paths such as OF and subsurface storm flow through macropores. S_u receives P_e. There are three fluxes leaving S_u: the actual evapotranspiration E_u, preferential streamflow Q_u, which directly contributes to the total streamflow Q_{tot}, and groundwater recharge Q_{us}, which feeds into the saturated reservoir S_s.
3. The saturated reservoir S_s: S_s represents the catchment's ground water reservoir. It receives Q_{us} and produces the groundwater flow Q_s, which contributes to the total streamflow Q_{tot}.

In the following, the above symbols will be used to describe both the name of a reservoir and the volume of water it contains. Volumes of water are treated as water heights in the model, being normalized by the geological entity's area while the water is in one of the reservoirs and by the catchment's total area once the water leaves the catchment.

The fluxes out of the reservoirs are calculated as follows: For evapotranspiration, a simple assumption is made. As long as there is sufficient water in S_i, E_i accounts for 50 % of E_p. If S_i contains less than 50 % of $E_p \cdot ts$, E_i equals S_i/ts. The remainder $((E_p - E_u) \cdot ts)$ can be taken from S_u, if sufficient water is available. ts is the model time step (1 h). If the amount of available water is less than the water stress threshold W_s, E_u is limited by the water availability according to Eq. (2):

$$E_u = \begin{cases} E_p - E_i & \text{if } S_u \geq W_s \\ (E_p - E_i) \cdot \dfrac{S_u}{W_s} & \text{otherwise} \end{cases} \quad (2)$$

The remaining fluxes, Q_u, Q_{us} and Q_s, are calculated using an empirical formula that depends on three calibrated parameters (Eq. (3)):

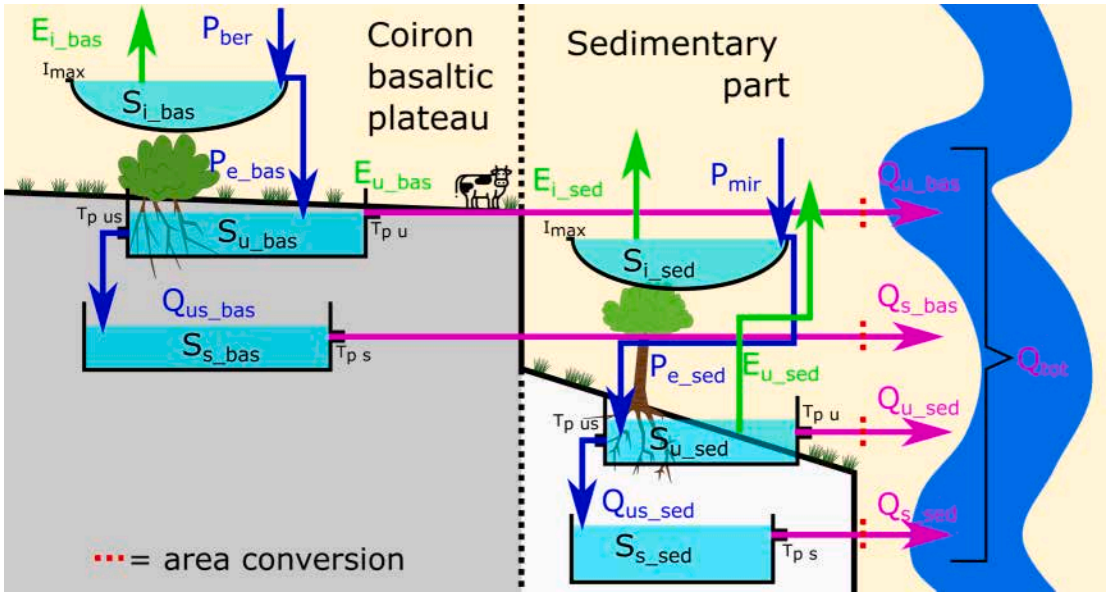

Fig. 3. Model reservoir structure. Water heights are respective to the geological entity's area and converted to the total catchment area once the water leaves the catchment.

$$Q = \begin{cases} \dfrac{S - \left(\left(-K{\cdot}ts + K{\cdot}ts{\cdot}A + \left(S - T_p\right)^{1-A} \right)^{\frac{-1}{A-1}} + T_p \right)}{ts} & \text{if } S > T_p \\ 0 & \text{otherwise} \end{cases} \quad (3)$$

A is a unitless parameter describing the non-linearity of the reservoir, where $A = 1$ corresponds to a linear reservoir (linear relation between Q and S). This formula is undefined for $A = 1$ but behaves quasi-linearly for A close to 1. Therefore, if $A = 1$, it is replaced by 1.0000000001. $A > 1$ signifies that an increase in storage leads to an overproportional increase in the outflow. K is a linear scaling factor: The higher K is, the faster the reservoir empties. T_p (in mm) is a threshold for outflow from the reservoir. It can alternatively be called a hydraulically passive part of the reservoir.

2.3.2. Age of water

The age of water is defined to be zero when it enters the catchment via effective precipitation. It then ages one hour every time step until leaving the catchment through streamflow. This age of water is tracked throughout the catchment. Accordingly, the amount of water in each reservoir at any time t is a distribution of water of different ages T, denoted as $S(T,t)$. The same is true for the fluxes, which have an age distribution $Q(T,t)$.

Water of different ages is not evenly distributed throughout each reservoir. Accordingly, the age distribution of fluxes out of a reservoir can differ significantly from the age distribution inside the reservoir. This is represented inside the model using SAS functions. We follow a procedure proposed by Van Der Velde et al. (2012), expressing the SAS function ω_Q^* (pdf) or Ω_Q^* (cdf) as a function of the cumulative age distribution in storage $P_S(T,t)$ instead of the age T (Eq. (4)). At a time t, Ω_Q^* gives the value of $P_Q(T,t)$ for a given $P_S(T,t)$. In the literature, this is often referred to as fractional SAS (fSAS) functions (Harman, 2015):

$$P_Q(T,t) = \Omega_Q^*(P_S(T,t),t) = \int_{P_S=0}^{P_S} \omega_Q^*(P_S(T,t),t) \quad (4)$$

In other words; the cumulative fSAS function $\Omega_Q^*(P_S,t)$ is the cumulative age distribution of a flux $P_Q(T,t)$ mapped to the cumulative storage age distribution P_S instead of the age T (at time t). This allows the use of a smooth mathematical function to approximate the SAS function for non-continuous $S(T,t)$ (i.e., variable amounts of water of each age, including ages without any water of that age). This means that the preference concerns the youngest x percent of the available water instead of all water younger than a fixed age.

In the model, a beta distribution (Eq. (5)) is used to approximate the SAS function:

$$f(x,a,b) = \frac{\Gamma(a+b){\cdot}x^{a-1}{\cdot}(1-x)^{b-1}}{\Gamma(a){\cdot}\Gamma(b)} \quad (5)$$

where Γ is the gamma function (Eq. (6)):

$$\Gamma(z) = \int_0^\infty y^{z-1}{\cdot}e^{-y}dy \quad (6)$$

Of the two shape parameters of the beta distribution a and b, a is calibrated, while b is fixed to 1. In the following, a is called SAS_α. This way, the gradient in age preference is strongest for the youngest water. $SAS_\alpha < 1$ corresponds to a young water preference, while $SAS_\alpha > 1$ corresponds to an old water preference. The beta distribution has the advantages of being defined for the interval $x \in [0,1]$ and having an integral of 1, making it convenient to use. Mathematically, the SAS sampling of any flux Q from a reservoir S is conducted as follows:

1. The cdf of the reservoir's age distribution is calculated: $P_S(T,t) = \int_{T=0}^{T} \frac{S(T,t)}{S(t)}$.
2. The SAS function is applied to calculate the cdf of the flux Q's age distribution: $P_Q(T,t) = \Omega_Q^*(P_S(T,t),t)$.
3. The absolute age distribution in the flux is calculated: $Q(T,t){\cdot}ts = p_Q(T,t){\cdot}Q(t){\cdot}ts = \frac{dP_Q(T,t)}{dT}{\cdot}Q(t){\cdot}ts$.
4. The absolute age distribution of the remaining water in storage is calculated: $S(T,t+1) = S(T,t) - Q(T,t){\cdot}ts$.

For a very strong young water preference and a high flux, this can lead to $Q(T,t){\cdot}ts > S(T,t)$ for the youngest ages, particularly when a short time step is used. In this case, the surplus of water is taken from the following ages that still contain water.

The SAS function is assumed to be invariant for E_u and Q_s, and SAS_α is calibrated directly. The age preference of fluxes out of the unsaturated zone is assumed to depend on the wetness condition of the unsaturated zone (Harman, 2015). Therefore, for Q_u and Q_{us}, a wetness-dependent SAS_α is applied. We assume a young water preference in both fluxes as

long as preferential flow occurs ($S_u > T_{pu}$). This young water preference is assumed to be stronger, when the unsaturated zone is wetter. An old water preference is assumed when S_u is below the preferential flow threshold T_{pu} and matrix flow should be the dominant mechanism, pushing out older water first. For Q_u and Q_{us}, SAS_α is calculated at each time step as a function of S_u using a calibrated scale factor $SAS_{stretch}$ (Eq. (7)). SAS_α is limited to a lower boundary of 0.2 in order to not obtain an unrealistically extreme young water preference:

$$SAS_\alpha = \begin{cases} 1 - \dfrac{S_u - T_{pu}}{SAS_{stretch}} & if 1 - \dfrac{S_u - T_{pu}}{SAS_{stretch}} > 0.2 \\ 0.2 & otherwise \end{cases} \quad (7)$$

This approach is similar to that used by Harman (2015) but uses the storage's preferential flow threshold as a point of no age preference. The utilization of SAS functions in a semi-distributed conceptual model with serial reservoirs comes with a challenge. The age preference of a flux out of a certain reservoir should be defined with regard to the time the water passed inside this reservoir and not with regard to the overall time spent inside the catchment. The final variable of interest, however, is the overall time spent inside the catchment and not only in the last reservoir. Therefore, for the saturated zone reservoir S_s receiving water at a certain age, both of these pieces of information are stored for each volume of water in the form of a 2D matrix until the water leaves S_s. In order to limit the computational demand of the model, the age of water is differentiated only for one year. All older water is assigned an age of one year. This choice was made because the objective of the model focuses on short transit times from a few hours to a few weeks. Furthermore, the chosen tracers and their dynamics are not expected to carry sufficient information to differentiate the age at a high temporal resolution beyond an age of one year.

2.3.3. Tracers

A tracer model version is used for calibration. Two tracers are used with different principles. Observations of δ^2H in precipitation are used as one of the model inputs. All of the precipitation that falls over one hour is assigned the average value of that hour (see subsection 2.2 for details). This signature is conserved throughout the entire water transfer through the model. The signature of the water leaving the catchment through streamflow is calculated from the signatures of all water contributing to streamflow at each moment. This signature is then compared to stream water analyses for calibration and validation. $[Si]$ is used as a second age tracer in a different manner. In precipitation, $[Si] = 0\ mg\ l^{-1}$. Dissolved silica originates from the dissolution of minerals in the saturated and unsaturated zone reservoirs as a function of the contact time and contact surface. A first-order dissolution kinetic from an infinite reservoir is assumed. The saturated and unsaturated zone reservoirs of each of the two geological entities each have a dissolution rate constant k that is obtained through calibration. k is calibrated independently for each reservoir in each geological entity. The mass of dissolved silica at time t, $mSi(t)$ in mg m^{-2}, is calculated from the mass and concentration of dissolved silica at the previous time step, $mSi(t-1)$ and $[Si](t-1)$, and the dissolved silica concentration at saturation $[Si]_{sat}$ using Eq. (8):

$$m_{Si}(t) = m_{Si}(t-1) + k \cdot ts \cdot \left(1 - \frac{[Si](t-1)}{[Si]_{sat}}\right) \quad (8)$$

This assumes that the (unknown) contact surface between water and soil minerals, which governs the dissolution rate, does not significantly vary with the water content in a reservoir, as the mass added is independent of the amount of water in the reservoir. This assumption is made because in the driest state, the smallest pores are still filled with water, and they account for most of the contact surface (due to their greater specific surface area). With regard to transfer, dissolved silica is treated as conservative, meaning that $[Si]$ in each flux and each age corresponds to $[Si]$ of the corresponding age in the corresponding reservoir that the flux originates from. The only exception is evapotranspiration: $[Si]$ in E_u is set to zero and the mass of dissolved silica in S_u remains the same, corresponding to the process of evapo-concentration. If no water of a certain age remains in S_u, the amount of dissolved silica for this age is set to zero, corresponding to the precipitation of the remaining silica.

2.3.4. Model calibration

In order to parametrize the processes described in the model, a set of 20 parameters (Table 1) is calibrated. We defined the parameter ranges based on prior assumptions, manual testing and first calibration runs with wider parameter ranges. Most parameters were chosen from a uniform distribution within the range. The silica dissolution rate constants and the reactivity parameter K from Eq. (3) were chosen from a uniform distribution in logarithmic space. A flow delay parameter (bas_{delay}; additional delay before adding water from the basaltic plateau to streamflow at the outlet) was chosen from integers. The calibration was performed by running the model repeatedly for 240 h on a 32-core node, corresponding to 76,907 model runs. Calibration was performed on the period from 2019 to 12-01 to 2020–12-31.

The calibration was used to maximize the Nash-Sutcliffe efficiency

Table 1
List of all calibrated model parameters with units, range and distribution from which they are chosen (uni = uniform, log = uniform in logarithmic space, int = integer). Abbreviations: pref. = preferential, dis. const. = dissolution rate constant.

Parameter	Description	unit	min	max	distr.
I_{max}	Size of interception reservoir	mm	0	3	uni
W_s	Water stress threshold	mm	50	200	uni
K_u	Unsaturated reservoir preferential flow reactivity	h^{-1}	5E-06	2E-04	log
A_u	Unsaturated reservoir pref. flow non-linearity	–	2	4.8	uni
$T_{p\ u}$	Unsaturated reservoir pref. flow threshold	mm	50	150	uni
K_{us}	Unsaturated reservoir recharge reactivity	h^{-1}	7E-06	1E-04	log
A_{us}	Unsaturated reservoir recharge non-linearity	–	2	4	uni
$T_{p\ us}$	Unsaturated reservoir recharge threshold	mm	40	100	uni
K_s	Saturated reservoir streamflow reactivity	h^{-1}	3E-07	1E-05	log
A_s	Saturated reservoir streamflow non-linearity	–	2	4	uni
$T_{p\ s}$	Saturated reservoir streamflow threshold	mm	200	1200	uni
$SAS_{\alpha\ Eu}$	Unsaturated reservoir ET SAS function	–	0.5	1	uni
$SAS_{\alpha\ u}$	Unsaturated reservoir pref. flow SAS function	–	0.5	1.7	uni
$SAS_{\alpha\ us}$	Unsaturated reservoir recharge SAS function	–	0.5	1.5	uni
$SAS_{\alpha\ s}$	Saturated reservoir streamflow SAS function	–	0.5	1.5	uni
$k_{Su\ bas}$	Unsaturated reservoir basalt Si dis. const.	$mg\ l^{-1}h^{-1}$	0.07	7	log
$k_{Su\ sed}$	Unsaturated reservoir sedimentary Si dis. const.	$mg\ l^{-1}h^{-1}$	0.006	0.6	log
$k_{Ss\ bas}$	Saturated reservoir basalt Si dis. const.	$mg\ l^{-1}h^{-1}$	0.1	10	log
$k_{Ss\ sed}$	Saturated reservoir sedimentary Si dis. const.	$mg\ l^{-1}h^{-1}$	0.01	1	log
bas_{delay}	Delay to outlet from basalt	h	0	2	int

(NSE; Eq. (9); Nash & Sutcliffe, 1970) of Q, $[Si]$ and δ^2H at the outlet of the Claduègne catchment:

$$NSE = 1 - \frac{\sum_{t=1}^{nt}(V_m(t) - V_o(t))^2}{\sum_{t=1}^{nt}\left(V_o(t) - \overline{V_o}\right)^2} \quad (9)$$

$V_m(t)$ and $V_o(t)$ are the modeled and observed values of the variable at time t, $\overline{V_o}$ is its average (from observations) and nt is the number of time steps. The NSE of the three variables is maximized by minimizing the Euclidian distance ED between each NSE value and 1 (Eq. (10)):

$$ED = \sqrt{(1 - NSE(Q))^2 + (1 - NSE([Si]))^2 + (1 - NSE(\delta^2H))^2} \quad (10)$$

The objective function ED is minimized using sequential model-based optimization (SMBO). This is done via Python's hyperopt module with a tree-structured Parzen estimator approach (TPE; Bergstra et al., 2011, 2013). Parallelization is obtained via ray tune (Liaw et al., 2018) version 1.6. The calculation was performed on a 32-core node of the *Grenoble alpes Recherche Infrastructure de CAlcul intensif et de Données (GRICAD)* of the *Université Grenoble Alpes*.

The tracer observation data span a relatively short period (14 months). Therefore, only one flood event in November 2019 was excluded from the calibration period in order to be used as independent validation. Note that a limited precision of the modeled stream δ^2H is to be expected for this period, as precipitation δ^2H sampling started just before this event.

The initial conditions were set as follows (corresponding approximately to the conditions after spin-up): For both geological entities, $S_i = 0\ mm$, $S_u = 50\ mm$, $S_s = 500\ mm$, δ^2H (all reservoirs) $= -45‰$ and $[Si](S_u) = 5 mg l^{-1}$. $[Si](S_s)$ was 15 mg l^{-1} for the basalt and 10 mg l^{-1} for the sedimentary part. The model is not very sensitive to the initial conditions, as they are adapted through the spin-up period. Regarding boundary conditions, there were no fluxes other than those presented above.

2.3.5. Age tracking

After calibration, the best-fit parameter set is used to run the age tracking version of the model. This version keeps track of the age distribution in each reservoir and flux at each moment in time. It takes significantly longer to run (a few days versus 3–4 min), as much more data are treated. The major increase in the calculation time is due to the preservation of current-state age information along two dimensions (since catchment entry and since reservoir entry) for water in the saturated reservoir. Another large factor is that instead of only treating the current state of each reservoir and flux, the whole history is tracked.

The main result is the TTD at any time during the model period $p_Q(T, t)$ for the overall streamflow at the outlet, as well as for the different contributions (Q_{ubas}, Q_{used}, Q_{sbas}, Q_{ssed}). In addition, the model calculates the RTD at any time during the model period for the whole catchment as well as for the different reservoirs (S_{ubas}, S_{used}, S_{sbas}, S_{ssed}). The TTDs of the whole model period can be summarized by the master TTD in its cumulative form, $P_{Qm}(T)$, which is calculated based on Eq. (11) and corresponds to the discharge-weighted average TTD:

$$P_{Qm}(T) = \frac{\sum_{t=0}^{nt-1} Q(T,t)}{\sum_{t=0}^{nt-1} Q(t)} \quad (11)$$

In the same way, the volume-weighted average RTD $P_{Sm}(T)$ can be calculated based on Eq. (12):

$$P_{Sm}(T) = \frac{\sum_{t=0}^{nt-1} S(T,t)}{\sum_{t=0}^{nt-1} S(t)} \quad (12)$$

In order to look at the temporal evolution of the TTDs, the fraction of water below a certain age can be considered. We focus on the ywf (younger than 30 d) and the nwf (younger than 1 d) in order to evaluate their evolution over time.

2.3.6. Sensitivity analysis

Due to the high number of calibrated parameters, different combinations of parameter values can lead to similarly good fits with regard to the streamflow discharge and tracers (equifinality). The predicted age results themselves cannot be verified, as the age distribution in the streamflow cannot be measured. The essential question with regard to the robustness of the predicted TTDs is the following: Do they vary strongly between different parameter sets that produce a good model fit? Therefore, the age results of different parameter sets that produced a good model fit ($ED < 0.7$, 4756 parameter sets in total) were assessed. As the age tracking model version is computationally demanding, the number of parameter sets to test had to be limited. In order to have a high chance to cover most of the possible variations, for each parameter, the parameter set with the highest value and that with the lowest value (of this parameter) were chosen (from those with $ED < 0.7$). bas_{delay} was not considered, as its value was 0 for all good fits. This resulted in 38 (2·19) parameter sets, the TTDs of which were compared. This makes it possible to approximate the uncertainty in the age results due to equifinality.

In addition, a simplified version of the model was tested that had constant SAS functions for each reservoir calibrating SAS_α directly for each of the fluxes (same number of calibration parameters). This served to evaluate whether the adaptive SAS-functions represent an advantage compared to fixed SAS functions. The calibration was also performed by running the model repeatedly for 240 h on a 32-core node, corresponding to 74,613 model runs.

The age results obtained from those different model parametrizations are compared with regard to the following metrics:

- $P_{Qm}(30d)$: the master ywf, the overall fraction of streamflow younger than 30 days;
- $P_{Qm}(1d)$: the master nwf, the overall fraction of streamflow younger than 1 day;
- ywf_{max}: the maximum ywf at any time within the model period;
- nwf_{max}: the maximum nwf at any time within the model period;
- $ywf_{max-24h}$: the maximum ywf integrated over 24 h of streamflow at any time within the model period;
- $nwf_{max-24h}$: the maximum nwf integrated over 24 h of streamflow at any time within the model period.

The 24 h integrated values are water-volume-weighted and not time-weighted. $nwf_{max-24h}$ is the maximum of all 24 h integrated nwfs at any time t (rolling window), $nwf_{24h}(t)$, and the equivalent value is calculated for $ywf_{max-24h}$. They are calculated based on Eq. (13) and Eq. (14):

$$nwf_{24h}(t) = \frac{\int_{t=t}^{t+23h}\int_{T=0}^{T+23h} Q(T,t)\,dT\,dt}{\int_{t=t}^{t+23h} Q(t)\,dt} \quad (13)$$

$$ywf_{24h}(t) = \frac{\int_{t=t}^{t+23h}\int_{T=0}^{T+719h} Q(T,t)\,dT\,dt}{\int_{t=t}^{t+23h} Q(t)\,dt} \quad (14)$$

3. Results & discussion

3.1. Tracer results & model fit

The obtained model fit after calibration results in an ED of 0.678 and NSEs for Q, $[Si]$ and δ^2H of 0.719, 0.634 and 0.504, respectively, for the calibration period. If we include the non-calibrated event, the ED is improved to 0.648 and the NSE values are 0.828, 0.631 and 0.495 for Q, $[Si]$ and δ^2H, respectively. This corresponds to a good to very good fit for the discharge and solutes according to Moriasi et al. (2015). The significant improvement of $NSE(Q)$ when the validation event is included is partially due to the high amplitude in discharge during this event, facilitating high NSE values. The relation between the modeled and observed values for the three parameters (Q, $[Si]$ and δ^2H) is shown in

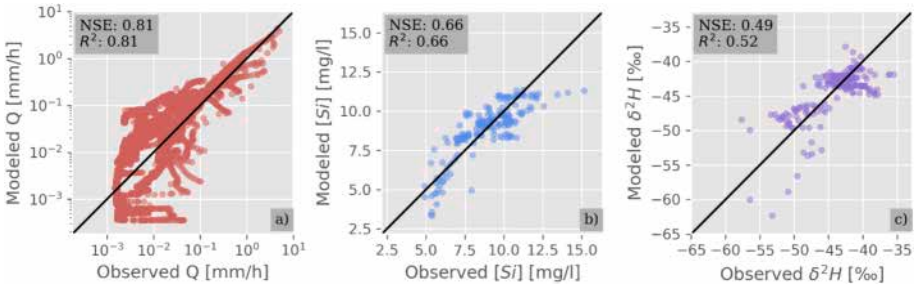

Fig. 4. Modeled versus observed a) streamflow discharge (***Q***), b) silicon concentration ([***Si***]) and c) deuterium ratio ($\boldsymbol{\delta^2 H}$) for the best fit. The figure includes the whole (calibration + validation) period. The black lines represent y = x. Note the log–log scale in panel a.

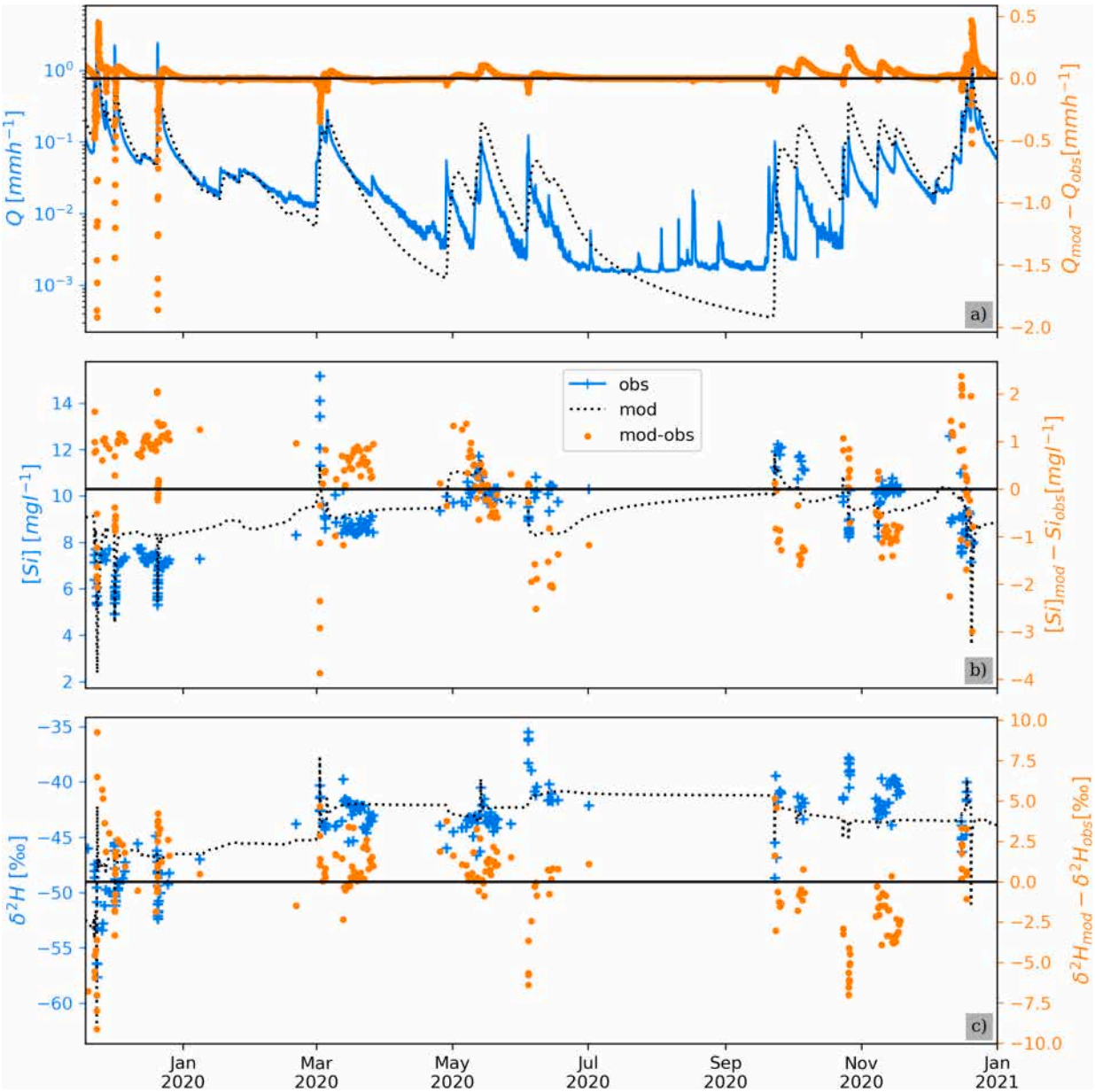

Fig. 5. Time series of modeled and observed values, as well as residuals (modeled – observed), of a) discharge (***Q***), b) dissolved silica concentration ([***Si***]) and c) deuterium isotope ratio ($\boldsymbol{\delta^2 H}$) for the best fit.

Fig. 4, including *NSE* and the coefficient of determination R^2 (Krause et al., 2005).

Fig. 5 shows the time series of modeled and observed values, as well as the residuals (modeled – observed) of *Q*, [*Si*] and δ^2H. A full time series and panels that zoom in on four individual events are provided in Supplemental Figs. S2 and S3. Concerning Q, the model reproduces

most of the largest flood events well. Most of the smaller flood events are well represented with regard to their amplitude, except the first autumn floods in October–November 2020, the amplitude of which is overestimated. The model, however, fails to reproduce well the rapid dynamics of flood events under dry conditions in summer. For most of these events (May to November), the peak discharge is underestimated and the discharge during the recession period is overestimated (Fig. 5a). The systematic character of this behavior can also be seen in Fig. 4a in the spikes to the right of the $y = x$ – line and the rounder shapes on the left of the $y = x$ – line. Looking at the contributions of the different reservoirs during these periods (data not shown here), the model does not produce preferential flow, as the unsaturated reservoir is filled below the preferential flow threshold. In terms of physical processes, the observed rapid flow may correspond to infiltration excess OF (IEOF), which is not represented in the model. IEOF might be enhanced through soil water repellency under dry conditions. Another observation is that the model underestimates the lowest flow under very dry conditions, which in observed data seems not to drop below a certain threshold. These are very low values (about $20ls^{-1}$) that may be partially explained by anthropogenic sources not accounted for in the model (e.g., waste water treatment plant effluent) or a natural very slow reservoir that has low relevance with regard to the overall flow but is relevant in the driest part of the year. During this very dry period (July to August), the observations show some small spikes in flow after small rain events, that are not reproduced by the model. They represent small total water volumes that might be explained by direct precipitation on streams or sealed surfaces (e.g., roads), a process that is not represented in the model.

The general patterns of $[Si]$ are reproduced well by the model (Fig. 5b). The flood events for which a dilution of $[Si]$ was observed follow this trend (e.g., large floods in autumn 2019) and during flood events for which an increase of $[Si]$ was observed, this pattern is also reproduced by the model (e.g., small floods in March, May, September and October 2020). The amplitude of $[Si]$ variations is sometimes overestimated (e.g. last flood event in December 2020) and sometimes underestimated (e.g. small flood in March 2020) by the model. In winter, the baseline of $[Si]$ is overestimated, but it matches the observations in summer. Fig. 4b shows that the model slightly underestimates the lowest $[Si]$ values. This means that the modeled "dilution" during the strongest rain events is a little too strong. This might indicate that the simple relation applied between SAS_α and S_u (Eq. (7)) is not fully realistic, even though it is better than assuming constant SAS functions (NSE = 0.66 vs. NSE = 0.59 for $[Si]$ from the best fit of adaptive vs. invariant SAS functions). The model more strongly underestimates the highest $[Si]$ values, which occurred during the flood event in March 2020. This, however, seems to be a unique case, so it is difficult to determine the origin of the observed spike in $[Si]$. Overall, the use of $[Si]$ as a second age tracer adds valuable information through its strong signal at the event scale.

Concerning δ^2H, the seasonal variations are captured well (Fig. 5c). The dynamics and amplitude of short-term variations are, however, not always well covered. It should be remembered that precipitation sampling for stable water isotope analyses started in November 2019, leading to a less robust isotopic signature in the modeled reservoirs at the beginning of the period. In addition, the precipitation sampler was completely filled during the event on the 23rd of November 2019 and the last 57 mm of precipitation could not be sampled. This leads to bad values during the end of the event. These two factors lead to a worse fit of modeled vs. observed δ^2H for the lowest values, which represent this event (Fig. 4c). During winter 2020/2021, some precipitation samples were missing due to damage caused by wild pigs and had to be interpolated, again leading to a higher uncertainty during this period.

The model version with time-invariant SAS functions resulted in a slightly worse *ED* (than that with adaptive SAS functions) for the calibration period (0.682) and a significantly worse ED for the whole period (0.723). Visual verification could show that the adaptive SAS functions increased (and thereby improved) the reactivity of tracer signatures during flood periods.

3.2. Modeled transit times

Fig. 6a shows the master transit time distribution $P_{Qm}(T)$ of the total streamflow discharge of the Cladugne catchment, as well as the different fluxes of the model. Out of all water that left the catchment during the observation period, 2.4 % spent less than 1 h in the catchment, 8.6 % spent less than 1 d in the catchment, 26 % spent less than 30 d in the catchment and 54 % spent less than 1 year in the catchment. It can be noted that the transit times of water leaving the catchment via direct flow from the unsaturated reservoirs (preferential flow) are much shorter than those for the overall streamflow. Here, 77 % and 89 % (basaltic and sedimentary parts, respectively) leave the catchment in less than 30 days. The two preferential flows account for only 14 % of the total amount of water leaving the catchment but represent 88 % of the new water (<1 d) and 44 % of the young water (<30 d) leaving the catchment. Fig. 6b relates P_{Qm} to P_{Sm}. This corresponds to the cumulative representation of the overall fSAS function (a volume-weighted time-average of $\Omega_Q^*(P_S, t)$) of the Cladugne catchment, as well as the different fluxes of the model. The figure reveals an overall young water preference of all fluxes (convex shape of all curves) that is stronger in preferential flow than in flow from the saturated zone. A slope > 1 corresponds to a preference, while a slope < 1 represents a disfavor. Over the whole observation period, there is a preference for the youngest 13 % of water in the catchment (slope > 1).

When looking at the fSAS function at the catchment scale at an individual moment under different conditions (wet vs. dry), this young water preference is increased under wet conditions and decreased under dry conditions. Under the driest conditions, there is a "disfavor" for the youngest water due to a disconnection of the unsaturated zone from the outflow (see Supplemental Fig. S5). This suggests the presence of an ISE in the Cladugne catchment. This is coherent with the results from Rodriguez et al. (2018) in a forested catchment under a Mediterranean climate. Directly comparing the catchment-scale SAS functions to those obtained by Rodriguez et al. (2018) is of limited interpretability due to a very different model structure. Rodriguez et al. (2018) use a model with one fast reservoir and one slow reservoir but no age preferences in each reservoir (complete mixing hypothesis). This leads to preferences for either all ages in the fast reservoir or all ages in the slow reservoir. Our model includes SAS functions (age preferences) inside each of the reservoirs, which are adaptive in the fast reservoirs. Therefore, age preferences are much "steeper" and more variable in our model. In contexts like the Cladugne catchment with its dynamic hydrology and flash floods, this adaptivity of age preferences, particularly for young water seems important.

We calculated χ (Eq. (15); equation (14) in Rodriguez et al. (2018)), an indicator of the ISE. We obtained a relatively high value (0.29 mm^{-1}, compared to 0.065 mm^{-1} obtained by Rodriguez et al. (2018)). This can also be explained by the different model structure, leading to a strong variability in the age preference for the very youngest ages in our model, as χ is calculated on the SAS function of the youngest age only:

$$\chi = \frac{\omega(P_S = 0, t_{max}) - \omega(P_S = 0, t_{min})}{S_{max} - S_{min}} \tag{15}$$

where t_{max} and t_{min} are the times of maximum and minimum catchment storage and S_{max} and S_{min} are the maximum and minimum catchment storage in mm.

The evolution of the ywf and nwf over the model period, as well as one event, is shown in Fig. 7a and b respectively. Supplemental Fig. S4 shows some additional events. The ywf is between 0 % and 20 % in summer and between 10 % and 30 % during most of the winter season. It reaches up to 80 % during the peaks of large flood events. The nwf is 0 %

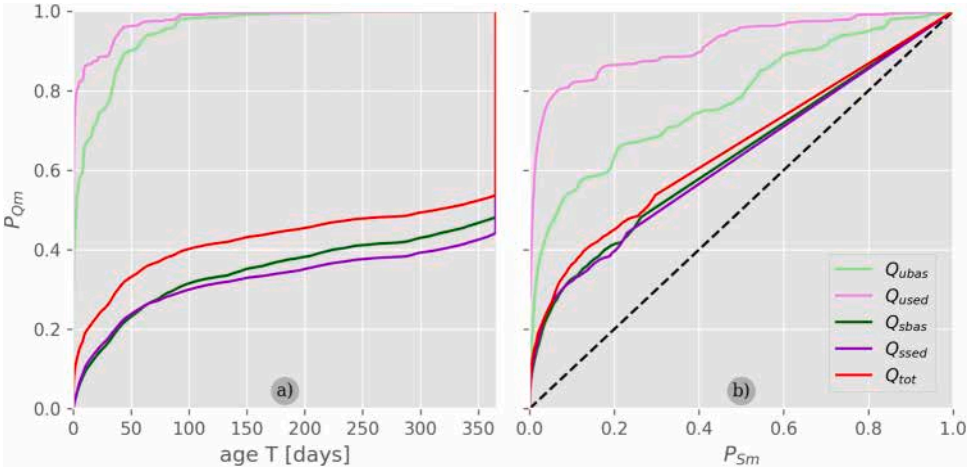

Fig. 6. A) master transit time distribution $\boldsymbol{P_{Qm}}$ of streamflow and its four contributions as a function of age T. b) $\boldsymbol{P_{Qm}}$ as a function of master residence time distribution $\boldsymbol{P_{Sm}}$ in streamflow and its four contributions. This corresponds to a cumulative representation of the discharge-weighted, time-averaged fractional StorAge Selection function Ω_Q^* (Eq. (4)).

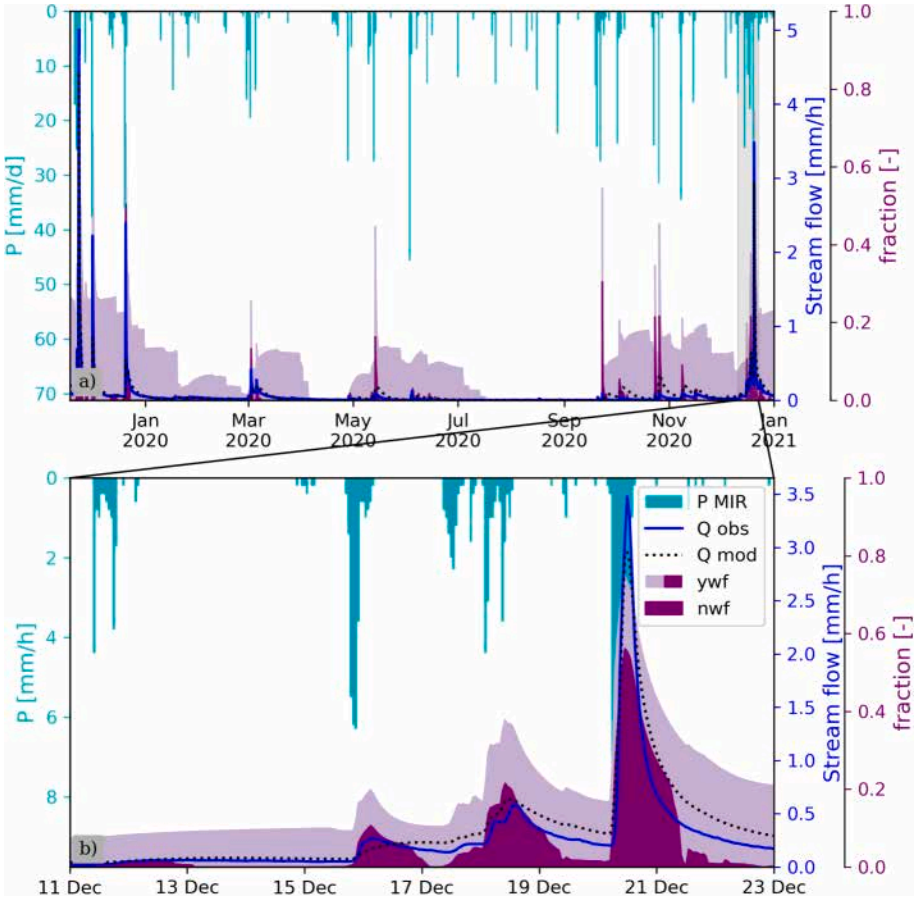

Fig. 7. Evolution of young water fraction (ywf; <30 d) and new water fraction (nwf; <1 d), as well as precipitation (P) and modeled and observed streamflow discharge (Q), over the whole modeled period and a major flood event. The ywf includes the nwf.

most of the time and shows short spikes during flood events that can reach up to 60 % for short periods of time during large flood events. This is in accordance with field observations of large-scale OF on the Coiron plateau during a large flood event (see Supplemental Fig. S1). The highly variable young water fractions are in accordance with results from Gallart et al. (2020) for a 0.56 km^2 Mediterranean catchment in the south-eastern Pre-Pyrenees (Spain). They found variable values for young water fractions (which they define by an age of 2–3 months) ranging from 0 to 1.

Fig. 8 summarizes the dependence of the nwf and ywf on discharge, classified in different flow regimes, in a similar manner to a figure presented by Gallart et al. (2020). It reveals two different relations below and above a streamflow of approximately 0.2 mm h^{-1} / approximately 2 m^3 s^{-1}, which is explained by the increasing contribution of

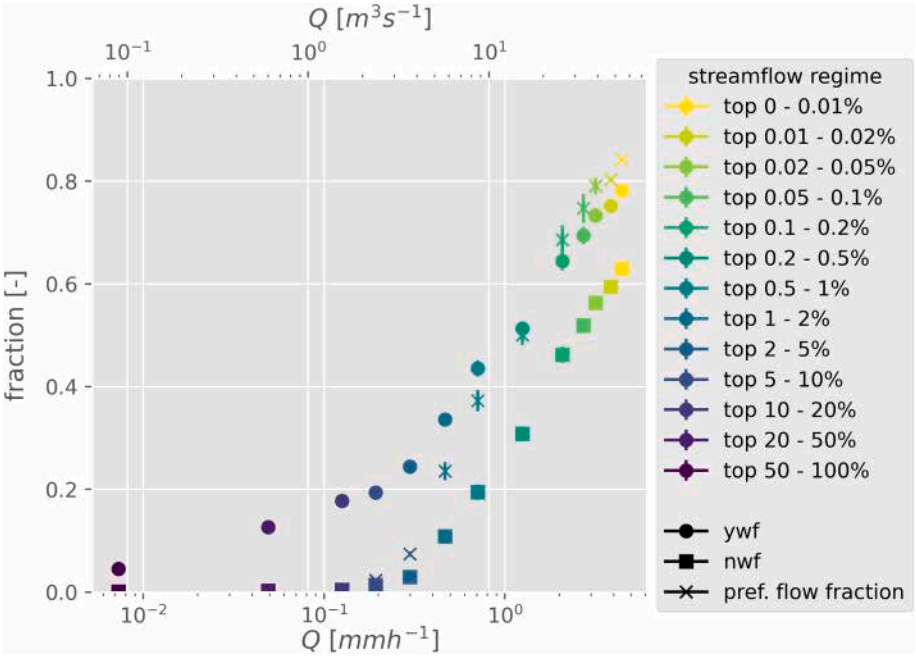

Fig. 8. Young water fraction (ywf; <30 d), new water fraction (nwf; <1 d) and fraction of preferential flow of different streamflow regimes as a function of streamflow discharge (Q). Note the logarithmic scale on the x-axis. Small horizontal and vertical bars (mostly covered by the markers) are the standard error.

preferential flow from the unsaturated reservoir above this threshold.

3.3. Sensitivity analysis

All 38 parameter sets from the sensitivity analysis produce similar results to those from the best fit with regard to the six tested age descriptors (Fig. 9, coefficient of variation < 8 %). This indicates that the predicted transit times are not very sensitive to the variations in the predicted parameter values between the different parameter sets that produce a good fit to the streamflow discharge and tracer observations. A complete list of parameter values and age results can be found in Supplemental Tables S1 and S2, respectively, and (Hachgenei et al., 2023). The model version with invariant SAS functions produces a slightly higher overall nwf $P_{Qm}(1d)$ and a lower maximum nwf (instantaneous (nwf_{max}) and integrated over 24 h ($nwf_{max-24h}$)). This is due to the missing adaptability to the wetness condition. The adaptive SAS functions produce a higher young water preference during strong flood events due to changes in flow paths, as well as a lower young water preference during drier periods. The predicted overall and instantaneous maximum ywf ($P_{Qm}(30d)$ and ywf_{max})) of the model version with invariant SAS functions is similar to that of the adaptive SAS functions model. The 24 h maximum ywf ($ywf_{max-24h}$) is higher using the model with invariant SAS functions. This is because the ywf remains high for longer compared to the adaptive SAS functions model, where the young water preference is highest only for a few hours during flood events.

3.4. Implications of the modeled TTD

The simulated TTDs suggest that large amounts of event water can reach the stream rapidly during flood events. The high temporal resolution of the model makes it possible to combine both seasonal and event-scale dynamics, which are both well-represented by the model for

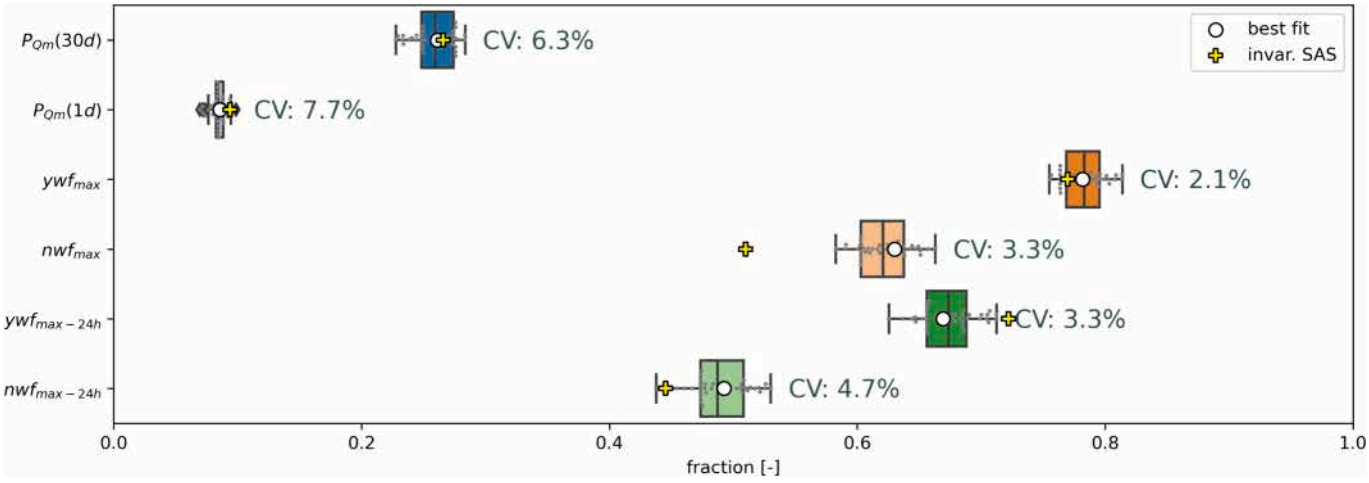

Fig. 9. Summary of age results from all 38 parameter sets from the sensitivity analysis (gray dots, boxes), compared to results from the best fit (white dot) and version of the model with invariant SAS functions (yellow cross). CV is the coefficient of variation. See subsection 2.3.6 for parameter description. (For interpretation of the references to colour in this figure legend, the reader is referred to the web version of this article.)

most cases.

The results indicate that there is a particular risk of the flushing of contaminants from soils into streams in the wet season (October–May), as this is the period with the highest young and new water fractions in the streamflow (Fig. 7), but even flood events in summer carry this risk. The model generally underestimates the reactivity of the catchment under dry conditions. The model produces no or very limited preferential flow Q_u under these conditions (data not shown). If we interpret this difference between the model and observations as the presence of preferential flow that is not represented by the model, the nwf and therefore the risk of contaminant mobilization under these conditions are likely to be higher in reality than expected from the model results.

3.5. Limitations of the model and possible improvements

One limitation of the model is its low reactivity to precipitation events on dry soil. The observed reactivity under these conditions is presumably due to preferential flow occurring under unsaturated conditions that is not represented in the model. It only concerns floods of small amplitude (observed discharge typically < 0.1 mm h^{-1}), but it is likely to affect the TTDs under these conditions. In the current model structure, all small pores need to be filled with water in order to generate preferential flow (the preferential flow threshold of the unsaturated reservoir T_{pu} physically represents the volume of small pores retaining water up to field capacity). Excess water above T_{pu} represents water flowing through macropores and OF. This representation is realistic under drying conditions due to capillary forces, preferentially holding water in small pores. During precipitation events on the other hand, this is not necessarily the case and two other types of processes may generate preferential flow: (1) Under wetting conditions, macropores may conduct water before all small pores are filled. (2) Soils have a limited infiltration capacity, and precipitation of an intensity exceeding the infiltration capacity may generate IEOF.

The current model is kept simple in order to limit the number of calibrated parameters, reduce equifinality and keep the computational demand low (computation time and memory usage). Both of the above processes could be implemented in a future version of the model, with the trade-off of requiring additional parameters and calculations. Furthermore, if additional reservoirs were used, the water age distributions for those reservoirs would need to be stored in memory and manipulated. In the Claduègne catchment, large flood events occur under wet conditions. Under these conditions, the small pores are saturated and the simple, current model structure is sufficient to reproduce such events. If a good representation of small flood events was needed, implementing the above processes could be useful.

Implementing the first process would require the unsaturated reservoir to be split in two (small and large pore spaces). Infiltration would be distributed into both spaces, so that the large pore space could contain water and produce rapid flow even under drier conditions. Under wet conditions (small pores saturated), all water would go into the large pore space, as is currently the case. The second process (IEOF) could be implemented in the model by adding an infiltration capacity and discharging any excess precipitation directly into the stream or having the water pass through a rapid infiltration excess reservoir that would physically correspond to water storage in depressions at the soil surface. An ongoing study of soils from the Claduègne catchment revealed water repellency under dry conditions, particularly for soils from the Coiron basaltic plateau. This water repellency could be represented by decreasing the infiltration capacity under very dry conditions (low S_u) or by using two different values for summer and winter.

In order to reproduce the very small discharge spikes in the driest period (Fig. 5a, July and August), some sealed surfaces directly contributing to streamflow discharge could be implemented. These spikes, however, represent an insignificant portion of the total streamflow and most likely originate from small urban areas. With regard to contaminants of agricultural origin, as well as with regard to the total streamflow, they are considered insignificant.

Assuming that δ^2H is a conservative tracer is not fully realistic, at least for the unsaturated zone, due to isotopic fractionation (Sprenger et al., 2018), mostly during evaporation and plant transpiration. This assumption was made in order to limit the model complexity.

Given the number of calibrated parameters, equifinality is a serious concern with different parameter sets being able to produce similarly good results. The approach used to limit this was constraining the model architecture, as well as parameter values, according to our knowledge of how the catchment functions, and limiting the total number of calibrated model parameters. For this purpose, lumped parameters were used for the hydrological parametrization of the reservoirs and for the SAS functions. The adaptive SAS functions were defined by only one calibration parameter, while the switch between young and old water preferences was fixed to the preferential flow threshold. A complementary strategy to limit equifinality was the use of two different tracers with different mechanisms in parallel. The sensitivity analysis showed that for different similarly good parameter sets, the obtained age results are very similar, even when the most diverse parameter sets are chosen. This indicates a certain robustness of the modeled age results with regard to equifinality.

There are several options to further reduce equifinality in a future version of the model by constraining model parameters. Silica dissolution rate constants could be fixed instead of being calibrated. This could be done by using hypotheses on the subsurface structure (soil and aquifer thickness, porosity and grain size distribution) and mineralogy, combined with literature values of dissolution rates. These hypotheses should be backed up with mineralogical analyses and/or experimental dissolution rates. While fixed dissolution rates would reduce equifinality by decreasing the number of parameters, the estimated value would remain uncertain due to a large uncertainty concerning the subsurface structure (actual contact surface), as well as large differences between laboratory and field dissolution rates (Swoboda-Colberg and Drever, 1993; Wild et al., 2019).

Another way to reduce equifinality would be to fix some of the hydrological parameters; in particular, the flow thresholds T_p (hydrologically passive storage) could be fixed. Concerning the preferential flow threshold T_{pu} (which represents the volume of small/medium pores of the soil that needs to be filled in order for the rapid, preferential flow Q_u to take place), a good estimation would be the field capacity of the soils. This parameter is relatively simple to obtain, as the necessary data are publicly available for the Claduègne catchment (Braud, 2015; Braud and Vandervaere, 2015). For the deeper, saturated reservoir, this estimation would be more complex, as T_p has no measurable physical equivalent. In addition to reducing equifinality, this manual parametrization would allow one to take into account the differences between the two geologies without adding calibration parameters.

Instead of reducing the calibration parameters, or in addition to doing this, equifinality could be reduced by constraining the model with further observations. Samples of groundwater sources from the two geological entities under dry conditions could be compared to the modeled signature of groundwater contributions to streamflow. Their fit could be added to the objective function during calibration.

In order to validate the model's applicability to another catchment and compare the Claduègne catchment to a forested catchment under a Mediterranean climate, the model could be adapted and applied to the Valescure catchment in the French Pyrenees. There is a comparable dataset for the Valescure catchment (Bouvier et al., 2018), which would allow the application of this model after some adaptation of its structure in order to represent its hydrological functions and hydrogeological structure well.

4. Conclusion

A tracer model with age tracking functionality was established for

the Claduègne catchment for a high temporal resolution of 1 h using two tracers subjected to different mechanisms. The high temporal resolution allowed insight into the intra-event dynamics of the nwf and ywf of flood events that are typically much shorter than a day in this catchment. At this timescale, the silicon tracer was a valuable indicator of event water in the stream. We could show that the nwfs and ywfs are particularly high during large flood events and the ywfs are generally higher over the autumn months. Our results confirm the ISE for this rural, agricultural catchment under a Mediterranean climate. The estimated transit times are very variable depending on the hydrological conditions. During large flood events (under very wet conditions), event water of a few hours of age is dominant, while under dry conditions (e.g., during most of the summer season), all water is older than 30 d and the majority is older than one year. In general, during the wet season (October–May), the fractions of new ($< 1\ d$) and young ($< 30\ d$) water are highest. This rapid transfer means little contact between the water and soil and thus less adsorption of contaminants. Therefore, the highest risk of the transfer of contaminants from the soil surface into the streams is expected during the wet season and generally during flood events. A sensitivity analysis showed little variability of the modeled TTD between the most dissimilar parameter sets that produce a good fit to the observed discharge and tracer data.

CRediT authorship contribution statement

Nico Hachgenei: Conceptualization, Data curation, Formal analysis, Investigation, Methodology, Resources, Software, Validation, Visualization, Writing – original draft, Writing – review & editing. **Guillaume Nord:** Investigation, Supervision, Writing – review & editing. **Lorenzo Spadini:** Investigation, Supervision, Writing – review & editing. **Patrick Ginot:** Data curation, Formal analysis, Resources. **Céline Voiron:** Data curation, Formal analysis. **Céline Duwig:** Formal analysis, Data curation.

Declaration of competing interest

The authors declare that they have no known competing financial interests or personal relationships that could have appeared to influence the work reported in this paper.

Code and data availability

The model code and forcing data, as well as the parameter values used in the sensitivity analysis, are published in Hachgenei et al. (2023).

Acknowledgements

We acknowledge the contribution of the technical services of IGE Laboratory for data acquisition. We are grateful to the AirOSol and PANDA platforms at IGE and the Geochemistry platform at ISTerre, for providing access to analytical facilities. The authors would like to acknowledge GRICAD (Grenoble Alpes Recherche - Infrastructure de Calcul Intensif et de Données) for access to calculation clusters and Mondher Chekki for his help in the deployment of the calculations. We thank Isabelle Braud for providing the potential evapotranspiration from the SAFRAN reanalysis.

Funding

The data used in this work were funded by the OHM-CV, which is a national observation service supported by the Institut National des Sciences de l'Univers and the Observatoire des Sciences de l'Univers de Grenoble. OHM-CV belongs to the OZCAR Research Infrastructure. The PhD project of Nico Hachgenei was financed by a scholarship granted by Université Grenoble Alpes.

Appendix A. Supplementary data

Supplementary data to this article can be found online at https://doi.org/10.1016/j.jhydrol.2024.131267.

References

Allen, R. G., Pereira, L. S., Raes, D., and Smith, M.: FAO Irrigation and Drainage Paper No. 56 - Crop Evapotranspiration, Rome Food Agric. Organ. United Nations, 56, 1998.

Benettin, P., Kirchner, J.W., Rinaldo, A., Botter, G., 2015a. Modeling chloride transport using travel time distributions at Plynlimon, Wales. Water Resour. Res. 51, 3259–3276. https://doi.org/10.1002/2014WR016600.

Benettin, P., Rinaldo, A., Botter, G., 2015b. Tracking residence times in hydrological systems: Forward and backward formulations. Hydrol. Process. 29, 5203–5213. https://doi.org/10.1002/hyp.10513.

Benettin, P., Soulsby, C., Birkel, C., Tetzlaff, D., Botter, G., Rinaldo, A., 2017. Using SAS functions and high-resolution isotope data to unravel travel time distributions in headwater catchments. Water Resour. Res. 53, 1864–1878. https://doi.org/10.1002/2016WR020117.

Berghuijs, W.R., Allen, S.T., 2019. Waters flowing out of systems are younger than the waters stored in those same systems. Hydrol. Process. 33, 3251–3254. https://doi.org/10.1002/hyp.13569.

Bergstra, J., Bardenet, R., Bengio, Y., and Kégl, B.: Algorithms for hyper-parameter optimization, Adv. Neural Inf. Process. Syst. 24 25th Annu. Conf. Neural Inf. Process. Syst. 2011, NIPS 2011, 1–9, 2011.

Bergstra, J., Yamins, D., Cox, D.D., 2013. Hyperopt : A Python Library for Optimizing the Hyperparameters of Machine Learning Algorithms. In: In: Proceedings of the 12th Python in Science Conference, pp. 13–19.

Beuerle, A., 2021. Implémentation d'un modèle conceptuel distribué pour simuler l'effet de la variabilité spatiale de la pluie sur les transferts de surface. Grenoble, France.

Blöschl, G., 2001. Scaling in hydrology. Hydrol. Process. 15, 709–711. https://doi.org/10.1002/hyp.432.

Botter, G., Bertuzzo, E., Rinaldo, A., 2010. Transport in the hydrologic response: Travel time distributions, soil moisture dynamics, and the old water paradox. Water Resour. Res. 46, n/a-n/a. https://doi.org/10.1029/2009WR008371.

Botter, G., Bertuzzo, E., Rinaldo, A., 2011. Catchment residence and travel time distributions: The master equation. Geophys. Res. Lett. 38, 1–6. https://doi.org/10.1029/2011GL047666.

Boudevillain, B., Delrieu, G., Galabertier, B., Bonnifait, L., Bouilloud, L., Kirstetter, P.-E., Mosini, M.-L., 2011. The Cévennes-Vivarais Mediterranean Hydrometeorological Observatory database. Water Resour. Res. 47, 1–6. https://doi.org/10.1029/2010WR010353.

Boudevillain, B., Delrieu, G., Wijbrans, A., Confoland, A., 2016. A high-resolution rainfall re-analysis based on radar–raingauge merging in the Cévennes-Vivarais region, France. J. Hydrol. 541, 14–23. https://doi.org/10.1016/j.jhydrol.2016.03.058.

Bouvier, C., Patris, N., Freydier, R., Guilhe-Batiot, C., Seidel, J.L., Taupin, J.D., Brunet, P., Remes, A., 2018. The Floodscale experiment in the small catchment of Valescure, France: An overview of the isotopic and geochemical data base. Geosci. Data J. 5, 14–27. https://doi.org/10.1002/gdj3.57.

Braud, I., 2015. Soil Properties Auzon Catchment. https://doi.org/10.6096/mistrals-hymex.1385.

Braud, I., Vandervaere, J.-P., 2015. Infiltration campaign Claduègne catchment, Ardèche. France. https://doi.org/10.6096/MISTRALS-HyMeX.1321.

Charuaud, L., Jardé, E., Jaffrézic, A., Liotaud, M., Goyat, Q., Mercier, F., Le Bot, B., 2019. Veterinary pharmaceutical residues in water resources and tap water in an intensive husbandry area in France. Sci. Total Environ. 664, 605–615. https://doi.org/10.1016/j.scitotenv.2019.01.303.

Danesh-Yazdi, M., Klaus, J., Condon, L.E., Maxwell, R.M., 2018. Bridging the gap between numerical solutions of travel time distributions and analytical storage selection functions. Hydrol. Process. 32, 1063–1076. https://doi.org/10.1002/hyp.11481.

Davies, J., Beven, K., Rodhe, A., Nyberg, L., Bishop, K., 2013. Integrated modeling of flow and residence times at the catchment scale with multiple interacting pathways. Water Resour. Res. 49, 4738–4750. https://doi.org/10.1002/wrcr.20377.

Delrieu, G., Nicol, J., Yates, E., Kirstetter, P.-E., Creutin, J.-D., Anquetin, S., Obled, C., Saulnier, G.-M., Ducrocq, V., Gaume, E., Payrastre, O., Andrieu, H., Ayral, P.-A., Bouvier, C., Neppel, L., Livet, M., Lang, M., Du-Châtelet, J.P., Walpersdorf, A., Wobrock, W., 2005. The catastrophic flash-flood event of 8–9 september 2002 in the gard region, france: a first case study for the cévennes-vivarais mediterranean hydrometeorological observatory. J. Hydrometeorol. 6, 34–52. https://doi.org/10.1175/JHM-400.1.

Fiori, A., Russo, D., 2008. Travel time distribution in a hillslope: Insight from numerical simulations. Water Resour. Res. 44, 1–14. https://doi.org/10.1029/2008WR007135.

Fovet, O., Ruiz, L., Hrachowitz, M., Faucheux, M., Gascuel-Odoux, C., 2014. Hydrological hysteresis in catchments and its value for assessing process consistency in conceptual models. Hydrol. Earth Syst. Sci. Discuss. 11, 5663–5707. https://doi.org/10.5194/hessd-11-5663-2014.

Gaillardet, J., Braud, I., Hankard, F., Anquetin, S., Bour, O., Dorfliger, N., de Dreuzy, J.R., Galle, S., Galy, C., Gogo, S., Gourcy, L., Habets, F., Laggoun, F., Longuevergne, L., Le Borgne, T., Naaim-Bouvet, F., Nord, G., Simonneaux, V., Six, D., Tallec, T., Valentin, C., Abril, G., Allemand, P., Arènes, A., Arfib, B., Arnaud, L., Arnaud, N., Arnaud, P., Audry, S., Comte, V.B., Batiot, C., Battais, A., Bellot, H., Bernard, E., Bertrand, C., Bessière, H., Binet, S., Bodin, J., Bodin, X., Boithias, L., Bouchez, J.,

Boudevillain, B., Moussa, I.B., Branger, F., Braun, J.J., Brunet, P., Caceres, B., Calmels, D., Cappelaere, B., Celle-Jeanton, H., Chabaux, F., Chalikakis, K., Champollion, C., Copard, Y., Cotel, C., Davy, P., Deline, P., Delrieu, G., Demarty, J., Dessert, C., Dumont, M., Emblanch, C., Ezzahar, J., Estèves, M., Favier, V., Faucheux, M., Filizola, N., Flammarion, P., Floury, P., Fovet, O., Fournier, M., Francez, A.J., Gandois, L., Gascuel, C., Gayer, E., Genthon, C., Gérard, M.F., Gilbert, D., Gouttevin, I., Grippa, M., Gruau, G., Jardani, A., Jeanneau, L., Join, J.L., Jourde, H., Karbou, F., Labat, D., Lagadeuc, Y., Lajeunesse, E., Lastennet, R., Lavado, W., Lawin, E., Lebel, T., Le Bouteiller, C., Legout, C., Lejeune, Y., Le Meur, E., Le Moigne, N., Lions, J., et al., 2018. OZCAR: The French network of critical zone observatories. Vadose Zo. J. 17 https://doi.org/10.2136/vzj2018.04.0067.

Gallart, F., Valiente, M., Llorens, P., Cayuela, C., Sprenger, M., Latron, J., 2020. Investigating young water fractions in a small Mediterranean mountain catchment: Both precipitation forcing and sampling frequency matter. Hydrol. Process. 34, 3618–3634. https://doi.org/10.1002/hyp.13806.

Ginn, T.R., Haeri, H., Massoudieh, A., Foglia, L., 2009. Notes on groundwater age in forward and inverse modeling. Transp. Porous Media 79, 117–134. https://doi.org/10.1007/s11242-009-9406-1.

Hachgenei, N., Nord, G., Spadini, L., Ginot, P., Voiron, C., and Duwig, C.: Water transit time tracing model using wetness adaptive StorAge Selection functions, https://doi.org/10.57745/OT1IFB, 2023.

Hachgenei, N., Vaury, V., Nord, G., Spadini, L., Duwig, C., 2022. Faster and more precise isotopic water analysis of discrete samples by predicting the repetitions' asymptote instead of averaging last values. MethodsX 9, 101656. https://doi.org/10.1016/j.mex.2022.101656.

Hachgenei, N.: Study of the distributed hydrologic response of the Claduègne catchment (Ardèche) using dense networks of rain and water level gauges, 60 pp., 2018.

Harman, C.J., 2015. Time-variable transit time distributions and transport: Theory and application to storage-dependent transport of chloride in a watershed. Water Resour. Res. 51, 1–30. https://doi.org/10.1002/2014WR015707.

Harman, C.J., Kim, M., 2014. An efficient tracer test for time-variable transit time distributions in periodic hydrodynamic systems. Geophys. Res. Lett. 41, 1567–1575. https://doi.org/10.1002/2013GL058980.

Heidbüchel, I., Troch, P.A., Lyon, S.W., Weiler, M., 2012. The master transit time distribution of variable flow systems. Water Resour. Res. 48, 1–19. https://doi.org/10.1029/2011WR011293.

Hrachowitz, M., Savenije, H., Bogaard, T.A., Tetzlaff, D., Soulsby, C., 2013. What can flux tracking teach us about water age distribution patterns and their temporal dynamics? Hydrol. Earth Syst. Sci. 17, 533–564. https://doi.org/10.5194/hess-17-533-2013.

Hrachowitz, M., Fovet, O., Ruiz, L., Euser, T., Gharari, S., Nijzink, R., Freer, J., Savenije, H.H.G., Gascuel-Odoux, C., 2014. Process consistency in models: The importance of system signatures, expert knowledge, and process complexity. Water Resour. Res. 50, 7445–7469. https://doi.org/10.1002/2014WR015484.

Hrachowitz, M., Fovet, O., Ruiz, L., Savenije, H.H.G., 2015a. Transit time distributions, legacy contamination and variability in biogeochemical 1/fα scaling: How are hydrological response dynamics linked to water quality at the catchment scale? Hydrol. Process. 29, 5241–5256. https://doi.org/10.1002/hyp.10546.

Hrachowitz, M., Fovet, O., Ruiz, L., Savenije, H.H.G., 2015b. Transit time distributions, legacy contamination and variability in biogeochemical 1/fαscaling: How are hydrological response dynamics linked to water quality at the catchment scale? Hydrol. Process. 29, 5241–5256. https://doi.org/10.1002/hyp.10546.

Hrachowitz, M., Benettin, P., van Breukelen, B.M., Fovet, O., Howden, N.J.K., Ruiz, L., van der Velde, Y., Wade, A.J., 2016. Transit times-the link between hydrology and water quality at the catchment scale. Wiley Interdiscip. Rev. Water 3, 629–657. https://doi.org/10.1002/wat2.1155.

INSEE, 2017. Recensement: https://www.insee.fr/fr/statistiques/zones/2011101?debut=0.

Jarvis, N.J., 2007. A review of non-equilibrium water flow and solute transport in soil macropores: Principles, controlling factors and consequences for water quality. Eur. J. Soil Sci. 58, 523–546. https://doi.org/10.1111/j.1365-2389.2007.00915.x.

Kim, M., Volkmann, T.H.M., Wang, Y., Meira Neto, A.A., Matos, K., Harman, C.J., Troch, P.A., 2022. Direct Observation of Hillslope Scale StorAge Selection Functions in Experimental Hydrologic Systems: Geomorphologic Structure and Preferential Discharge of Old Water. Water Resour. Res. 58, 1–27. https://doi.org/10.1029/2020WR028959.

Kirchner, J.W., Feng, X., Neal, C., 2000. Frail chemistry and its implications for contaminant transport in catchments. Nature 403, 524–527. https://doi.org/10.1038/35000537.

Kirchner, J.W., Feng, X., Neal, C., 2001. Catchment-scale advection and dispersion as a mechanism for fractal scaling in stream tracer concentrations. J. Hydrol. 254, 82–101. https://doi.org/10.1016/S0022-1694(01)00487-5.

Klaus, J., Chun, K.P., McGuire, K.J., McDonnell, J.J., 2015. Temporal dynamics of catchment transit times from stable isotope data. Water Resour. Res. 51, 4208–4223. https://doi.org/10.1002/2014WR016247.

Krause, P., Boyle, D.P., Bäse, F., 2005. Comparison of different efficiency criteria for hydrological model assessment. Adv. Geosci. 5, 89–97. https://doi.org/10.5194/adgeo-5-89-2005.

Liaw, R., Liang, E., Nishihara, R., Moritz, P., Gonzalez, J. E., and Stoica, I.: Tune: A Research Platform for Distributed Model Selection and Training, arXiv Prepr. arXiv1807.05118, 2018.

Małoszewski, P., Zuber, A., 1982. Determining the turnover time of groundwater systems with the aid of environmental tracers. 1. Models and their applicability. J. Hydrol. 57, 207–231. https://doi.org/10.1016/0022-1694(82)90147-0.

Maxwell, R.M., Condon, L.E., Kollet, S.J., Maher, K., Haggerty, R., Forrester, M.M., 2016. The imprint of climate and geology on the residence times of groundwater. Geophys. Res. Lett. 43, 701–708. https://doi.org/10.1002/2015GL066916.

McGuire, K.J., McDonnell, J.J., 2006. A review and evaluation of catchment transit time modeling. J. Hydrol. 330, 543–563. https://doi.org/10.1016/j.jhydrol.2006.04.020.

Meira Neto, A.A., Kim, M., Troch, P.A., 2022. Physical Interpretation of Time-Varying StorAge Selection Functions in a Bench-Scale Hillslope Experiment via Geophysical Imaging of Ages of Water. Water Resour. Res. 58 https://doi.org/10.1029/2021WR030950.

Moriasi, D.N., Gitau, M.W., Pai, N., Daggupati, P., 2015. Hydrologic and water quality models: Performance measures and evaluation criteria. Trans. ASABE 58, 1763–1785. https://doi.org/10.13031/trans.58.10715.

Nash, J.E., Sutcliffe, J., 1970. V: River Flow Forecasting Through Conceptual Models Part I-a Discussion of Principles. J. Hydrol. 10, 282–290. https://doi.org/10.1016/0022-1694(70)90255-6.

Niemi, A.J., 1977. Residence time distributions of variable flow processes. Int. J. Appl. Radiat. Isot. 28, 855–860. https://doi.org/10.1016/0020-708X(77)90026-6.

Nord, G., Boudevillain, B., Berne, A., Branger, F., Braud, I., Dramais, G., Gérard, S., Le Coz, J., Legoût, C., Molinié, G., Van Baelen, J., Vandervaere, J.P., Andrieu, J., Aubert, C., Calianno, M., Delrieu, G., Grazioli, J., Hachani, S., Horner, I., Huza, J., Le Boursicaud, R., Raupach, T.H., Teuling, A.J., Uber, M., Vincendon, B., Wijbrans, A., 2017. A high space-time resolution dataset linking meteorological forcing and hydro-sedimentary response in a mesoscale Mediterranean catchment (Auzon) of the Ardèche region, France. Earth Syst. Sci. Data 9, 221–249. https://doi.org/10.5194/essd-9-221-2017.

Nuissier, O., Ducrocq, V., Ricard, D., Lebeaupin, C., Anquetin, S., 2008. A numerical study of three catastrophic precipitating events over southern France. I: Numerical framework and synoptic ingredients. Q. J. r. Meteorol. Soc. 134, 111–130. https://doi.org/10.1002/qj.200.

Obimakinde, S., Fatoki, O., Opeolu, B., Olatunji, O., 2017. Veterinary pharmaceuticals in aqueous systems and associated effects: an update. Environ. Sci. Pollut. Res. 24, 3274–3297. https://doi.org/10.1007/s11356-016-7757-z.

OHMCV: Gazel and Claduègne hydro-sedimentary stations, https://doi.org/10.17178/OHMCV.HSS.CLA.11-14.1, 2011.

Ojoghoro, J.O., Scrimshaw, M.D., Sumpter, J.P., 2021. Steroid hormones in the aquatic environment. Sci. Total Environ. 792, 148306 https://doi.org/10.1016/j.scitotenv.2021.148306.

Remondi, F., Kirchner, J.W., Burlando, P., Fatichi, S., 2018. Water flux tracking with a distributed hydrological model to quantify controls on the spatiotemporal variability of transit time distributions. Water Resour. Res. 54, 3081–3099. https://doi.org/10.1002/2017WR021689.

Remondi, F., Botter, M., Burlando, P., Fatichi, S., 2019. Variability of transit time distributions with climate and topography: a modelling approach. J. Hydrol. 569, 37–50. https://doi.org/10.1016/j.jhydrol.2018.11.011.

Rinaldo, A., Beven, K.J., Bertuzzo, E., Nicotina, L., Davies, J., Fiori, A., Russo, D., Botter, G., 2011. Catchment travel time distributions and water flow in soils. Water Resour. Res. 47, 1–13. https://doi.org/10.1029/2011WR010478.

Rinaldo, A., Benettin, P., Harman, C.J., Hrachowitz, M., McGuire, K.J., van der Velde, Y., Bertuzzo, E., Botter, G., 2015. Storage selection functions: a coherent framework for quantifying how catchments store and release water and solutes. Water Resour. Res. 51, 4840–4847. https://doi.org/10.1002/2015WR017273.

Rodhe, A., Nyberg, L., Bishop, K., 1996. Transit times for water in a small till catchment from a step shift in the oxygen 18 content of the water input. Water Resour. Res. 32, 3497–3511. https://doi.org/10.1029/95WR01806.

Rodriguez, N.B., McGuire, K.J., Klaus, J., 2018. Time-varying storage-water age relationships in a catchment with a mediterranean climate. Water Resour. Res. 54, 3988–4008. https://doi.org/10.1029/2017WR021964.

Rodriguez, N.B., Pfister, L., Zehe, E., Klaus, J., 2021. A comparison of catchment travel times and storage deduced from deuterium and tritium tracers using StorAge Selection functions. Hydrol. Earth Syst. Sci. 25, 401–428. https://doi.org/10.5194/hess-25-401-2021.

Segura, C., James, A.L., Lazzati, D., Roulet, N.T., 2012. Scaling relationships for event water contributions and transit times in small-forested catchments in Eastern Quebec. Water Resour. Res. 48, 1–21. https://doi.org/10.1029/2012WR011890.

Singh, S.K., Stenger, R., 2018. Indirect Methods to Elucidate Water Flows and Contaminant Transfer Pathways through Meso-scale Catchments – a Review. Environ. Process. 5, 683–706. https://doi.org/10.1007/s40710-018-0331-6.

Soulsby, C., Birkel, C., Geris, J., Dick, J., Tunaley, C., Tetzlaff, D., 2015. Stream water age distributions controlled by storage dynamics and nonlinear hydrologic connectivity: Modeling with high-resolution isotope data. Water Resour. Res. 51, 7759–7776. https://doi.org/10.1002/2015WR017888.

Sprenger, M., Stumpp, C., Weiler, M., Aeschbach, W., Allen, S.T., Benettin, P., Dubbert, M., Hartmann, A., Hrachowitz, M., Kirchner, J.W., McDonnell, J.J., Orlowski, N., Penna, D., Pfahl, S., Rinderer, M., Rodriguez, N., Schmidt, M., Werner, C., 2019. The demographics of water: a review of water ages in the critical zone. Rev. Geophys. 800–834 https://doi.org/10.1029/2018rg000633.

Swoboda-Colberg, N.G., Drever, J.I., 1993. Mineral dissolution rates in plot-scale field and laboratory experiments. Chem. Geol. 105, 51–69. https://doi.org/10.1016/0009-2541(93)90118-3.

Van Der Velde, Y., Torfs, P.J.J.F., Van Der Zee, S.E.A.T.M., Uijlenhoet, R., 2012. Quantifying catchment-scale mixing and its effect on time-varying travel time distributions. Water Resour. Res. 48, 1–13. https://doi.org/10.1029/2011WR011310.

van der Velde, Y., Heidbüchel, I., Lyon, S.W., Nyberg, L., Rodhe, A., Bishop, K., Troch, P. A., 2015. Consequences of mixing assumptions for time-variable travel time distributions. Hydrol. Process. 29, 3460–3474. https://doi.org/10.1002/hyp.10372.

Vidal, J.P., Martin, E., Franchistéguy, L., Habets, F., Soubeyroux, J.M., Blanchard, M., Baillon, M., 2010. Multilevel and multiscale drought reanalysis over France with the Safran-Isba-Modcou hydrometeorological suite. Hydrol. Earth Syst. Sci. 14, 459–478. https://doi.org/10.5194/hess-14-459-2010.

Weill, S., Lesparre, N., Jeannot, B., Delay, F., 2019. Variability of Water Transit Time Distributions at the Strengbach Catchment (Vosges Mountains, France) Inferred Through Integrated Hydrological Modeling and Particle Tracking Algorithms. Water 11, 2637. https://doi.org/10.3390/w11122637.

Wild, B., Daval, D., Beaulieu, E., Pierret, M.C., Viville, D., Imfeld, G., 2019. In-situ dissolution rates of silicate minerals and associated bacterial communities in the critical zone (Strengbach catchment, France). Geochim. Cosmochim. Acta 249, 95–120. https://doi.org/10.1016/J.GCA.2019.01.003.

Yang, J., Heidbüchel, I., Musolff, A., Reinstorf, F., Fleckenstein, J.H., 2018. Exploring the dynamics of transit times and subsurface mixing in a small agricultural catchment. Water Resour. Res. 54, 2317–2335. https://doi.org/10.1002/2017WR021896.

Zhang, Z., Chen, X., Cheng, Q., Soulsby, C., 2021. Using StorAge Selection (SAS) functions to understand flow paths and age distributions in contrasting karst groundwater systems. J. Hydrol. 602, 126785 https://doi.org/10.1016/j.jhydrol.2021.126785.